Human formin FHOD3-mediated actin elongation is required for sarcomere integrity in cardiomyocytes

Dylan A. Valencia[1], Angela N. Koeberlein[1], Haruko Nakano[2,3], Akos Rudas[4], Airi Harui[5], Cassandra Spencer[2], Atsushi Nakano[2,3,6*], and Margot E. Quinlan[1,6*]

[1]Department of Chemistry and Biochemistry, [2]Department of Molecular, Cell, and Developmental Biology, [3]Eli & Edythe Broad Center of Regenerative Medicine & Stem Cell Research, [4]Department of Computational Medicine, [5]Divison of Pulmonary & Critical Care Medicine, Geffen School of Medicine, [6]Molecular Biology Institute, University of California Los Angeles, Los Angeles, California, 90095

*To whom correspondence should be addressed: UCLA Department of Chemistry and Biochemistry, 607 Charles E. Young Dr. E., Los Angeles, California 90095. E-mail: anakano@ucla.edu, margot@chem.ucla.edu

Abstract

Contractility and cell motility depend on accurately controlled assembly of the actin cytoskeleton. Formins are a large group of actin assembly proteins that nucleate new actin filaments and act as elongation factors. Some formins may cap filaments, instead of elongating them, and others are known to sever or bundle filaments. The Formin HOmology Domain-containing protein (FHOD)-family of formins is critical to the formation of the fundamental contractile unit in muscle, the sarcomere. Specifically, mammalian FHOD3L plays an essential role in cardiomyocytes. Despite our knowledge of FHOD3L's importance in cardiomyocytes, its biochemical and cellular activities remain poorly understood. It has been proposed that FHOD-family formins act by capping and bundling, as opposed to assembling new filaments. Here, we demonstrate that FHOD3L nucleates actin and rapidly but briefly elongates filaments after temporarily pausing elongation, *in vitro*. We designed function-separating mutants that enabled us to distinguish which biochemical roles are req`uired in the cell. We found that human FHOD3L's elongation activity, but not its nucleation, capping, or bundling activity, is necessary for proper sarcomere formation and contractile function in neonatal rat ventricular myocytes. The results of this work provide new insight into the mechanisms by which formins build specific structures and will contribute to knowledge regarding how cardiomyopathies arise from defects in sarcomere formation and maintenance.

Keywords: Actin; Formin; Formin Homology Domain-Containing Protein 3 (FHOD3); Sarcomere; Cardiomyocyte; Hypertrophic cardiomyopathy (HCM)

Introduction

Higher order actin-based structures, such as the sarcomere, are the foundation for specific cellular functions that demand precise spatial and temporal coordination. Other examples of actin-based structures, including filopodia, stress fibers and the cytokinetic furrow, are also required for a wide range of processes, such as cell migration, adhesion, and division (Blanchoin et al., 2014; Svitkina, 2018). Hundreds of actin-binding proteins, and specific combinations thereof, coordinate to assemble these complex structures by accelerating actin assembly, crosslinking and bundling filaments, and stabilizing and/or disassembling actin filaments (Dominguez and Holmes, 2011; Lappalainen et al., 2022; Pollard, 2016). There are three known classes of actin nucleators that stimulate *de novo* filament assembly. Each class functions by a distinct mechanism, resulting in a unique starting point for the structure it initiates.

One such class of actin nucleators, known as formins, mediates both nucleation and continued elongation of actin filaments. Formins are defined by their Formin Homology (FH) domains 1 and 2. The FH2 domain is highly conserved and forms a donut-shaped homodimer, which is sufficient to nucleate new filaments. After nucleation, the FH2 domain remains processively associated with the faster-growing barbed-end of actin filaments, modifying the rate of elongation. The FH1 domain is less well conserved but contains proline-rich tracts that bind profilin-actin to facilitate elongation of actin filaments (Courtemanche, 2018; Paul and Pollard, 2008, 2009). The regulatory domains for most formins are on either side of these FH domains and an intramolecular interaction leads to autoinhibition (Goode and Eck, 2007; Li and Higgs, 2005; Schonichen and Geyer, 2010). The timing and strength of formin activity differ between formins, allowing for distinct roles within a given cell (Homa et al., 2021).

Multiple classes of formins have been linked to sarcomere structure, including Dishevelled Associated Activator Of Morphogenesis (Daam1, 2), Diaphanous (Diaph1-3), Formin HOmology Domain–containing protein (FHOD1, 3), and others (Deng et al., 2021; Iskratsch et al., 2010; Li et al., 2011; Mi-Mi et al., 2012; Molnár et al., 2014; Rosado et al., 2014; Sanger et al., 2017; Shwartz et al., 2016; Sundaramurthy et al., 2020; Taniguchi et al., 2009). There are two mammalian isoforms in the FHOD family of formins, FHOD1 and FHOD3 (Bechtold et al., 2014; Kanaya et al., 2005; Schonichen and Geyer, 2010). FHOD1 is widely expressed and assembles stress fibers that contribute to adhesion and motility of various cell types (Gasteier et al., 2003; Iskratsch et al., 2013; Koka et al., 2003; Schulze et al., 2014). Despite its localization to intercalated discs, structures important for rapid signal transmission and synchronized contractions, FHOD1 seems to be dispensable in cardiomyocytes (Al Haj et al., 2015; Dwyer et al., 2014; Sanematsu et al., 2019). In contrast, FHOD3 is implicated in sarcomere assembly and maintenance (Fujimoto et al., 2016; Iskratsch et al., 2010; Kan-o et al., 2012a; Taniguchi et al., 2009; Ushijima et al., 2018).

There are four isoforms of FHOD3 reported in Uniprot. The major differences are due to alternative splicing in the N-terminal half. An eight residue insert in the C-terminal half (an acidic sequence $T(D/E)_5XE$) is present only in Uniprot isoform 4, which is commonly referred to as FHOD3L (Iskratsch et al., 2010). In this paper, we adopt the commonly accepted nomenclature in which FHOD3S (short) indicates Uniprot isoform 1 and FHOD3L (long) indicates Uniprot isoform 4 (Figure 1). FHOD3L is predominantly expressed in striated muscle, whereas FHOD3S is more widely expressed (Taniguchi et al., 2009). In cardiomyocytes, FHOD3L localizes to sarcomeres in a striated pattern (Iskratsch et al., 2010; Kan-o et al., 2012b; Taniguchi et al., 2009). Interestingly, FHOD3L does not localize at the barbed end of actin filaments within sarcomeres. Instead, a direct interaction between FHOD3L and cardiac myosin-binding protein C (cMyBP-C) drives localization of FHOD3L to the so-called C zone of sarcomeres (Matsuyama et al., 2018a). In the absence of cMyBP-C, FHOD3L is diffuse and cardiac function is compromised, suggesting that a balance between these two proteins is critical for proper heart function in mice (Matsuyama et al., 2018a).

Mutations in the *FHOD3* gene have been deemed causative in at least 1-2% of patients with hypertrophic cardiomyopathy (HCM), in addition to cases of left ventricular noncompaction (LVNC), dilated cardiomyopathy (DCM), and progressive high-frequency hearing loss (Arimura et al., 2013; Boussaty et al., 2023; Myasnikov et al., 2022; Ochoa et al., 2018). Moreover, recent clinical studies have shown that HCM-causative FHOD3 mutations increase the risk of cardiovascular death and all-cause death, with the onset of the disease occurring as early as age 4 and as late as age 63 (Vodnjov et al., 2023; Wu et al., 2021).

Despite its known physiological significance, we lack a mechanistic understanding of FHOD3L's role in cardiac development and function. Early biochemical analysis suggested that FHOD family formins were an exceptional class of formins. Both purified mammalian isoforms (FHOD1 and FHOD3) were found to decelerate, rather than hasten, actin assembly *in vitro* (Schonichen et al., 2013; Taniguchi et al., 2009). In addition, actin bundling was observed for FHOD1 (Schonichen et al., 2013). Consistently, FHOD1 mediates nuclear movement by bundling and anchoring actin filaments (Antoku et al., 2023). However, it fails to complete this function when a highly conserved isoleucine in the FH2 domain is mutated (hereafter, referred to as the IA mutation) (Kutscheidt et al., 2014). The IA mutation is known to disrupt both nucleation and elongation in most, if not all, formins, indicating that FHOD1 may enhance actin assembly in addition to bundling *in vivo* (Patel et al., 2018; Xu et al., 2004). In addition, FHOD proteins are required to form new sarcomeres in rat cardiomyocytes, human induced cardiomyocytes, worms and mice (Fenix et al., 2018; Iskratsch et al., 2010; Kan-O et al., 2012; Sundaramurthy et al., 2020; Taniguchi et al., 2009). FHODs with the IA mutation do not form new sarcomeres, suggesting that actin assembly is required for sarcomere assembly, in conflict with the biochemical data (Kan-O et al., 2012; Shwartz et al., 2016; Taniguchi et al., 2009; Xu et al., 2004). Most recently, in the worm, FHOD protein was shown to cooperate with profilin to build muscle, providing strong evidence that it functions by elongating actin filaments (Kimmich et al., 2024). Previously, we found that *Drosophila* Fhod is a potent actin nucleator that can accelerate actin elongation under certain conditions (Patel et al., 2018). We also showed that human FHOD1 can nucleate actin but its activity is sensitive to the actin isoform (Patel et al., 2018). We confirmed that both of these Fhod-family formins lose activity when the IA mutation is introduced (Patel et al., 2018). Based on these biochemical results and the data regarding Fhod-family formins in muscle of multiple species, we asked whether human FHOD3L can also nucleate.

Here, we show that purified FHOD3L can accelerate actin assembly by both nucleation and elongation. We also confirm that FHOD3L potently caps filaments, in the absence of profilin, and bundles. Using function-separating mutations, we correlate FHOD3L's biochemistry to the integrity of the sarcomere within cardiomyocytes. We found that reduced nucleation, capping, and bundling by FHOD3L are well tolerated in neonatal rat ventricular myocytes (NRVMs), whereas elongation activity is necessary for proper sarcomere formation and function.

Results

Biochemical characterization of human FHOD3

We purified the C-terminal half of human FHOD3L (FHOD3L-CT), encompassing the FH1 domain, FH2 domain, and C-terminal tail, which is typically sufficient for actin assembly *in vitro* and *in vivo* (Figure 1, Figure 1—figure supplement 1) (Courtemanche, 2018; Patel et al., 2018). In contrast to an earlier report, we found that FHOD3L-CT enhances rabbit skeletal muscle actin (RSA) assembly in bulk pyrene assays (Figure 2A,B, Table 1) (Taniguchi et al., 2009). (Table 1 summarizes all biochemical measurements.) Consistent with nucleation activity, when we visualized the products of similar reactions, we observed many more filaments in the presence of FHOD3L-CT compared to actin alone (Figure 2—figure supplement 1A). We also asked if the shorter, alternatively spliced FHOD3 isoform, FHOD3S-CT, nucleates actin. FHOD3S-CT, which is 8 residues shorter than FHOD3L-CT, accelerates actin assembly ~30% more potently than FHOD3L-CT (Figure 2B, Figure 2—figure supplement 2A). Thus, we conclude that the C-terminal half of both FHOD3 isoforms (moving forward, we will use S/L

when indicating both the short and long isoforms of FHOD3) are able to nucleate actin filaments.

To further compare FHOD3L-CT to previously characterized formins, we introduced mutations at conserved residues of the FH2 domain, I1163A and K1309A (Xu et al., 2004). Like other formins, the I1163A mutant lacked nucleation activity and the K1309A mutant reduced nucleation by ~90% (Figure 2B). We observed a reduction in the plateau of pyrene traces with wild-type FHOD3S/L-CT and the mutants. The decrease was more apparent at higher concentrations of the nucleator and seemed to be dose-dependent (Figure 2A, Figure 2—figure supplement 2A). Control experiments demonstrated that the fluorescence change does not reflect quenching due to side binding or bundling (Figure 2—figure supplement 1B). We, therefore, tested barbed-end binding. We asked whether FHOD3L-CT inhibits filament elongation by performing bulk seeded-elongation assays. Indeed, we found that FHOD3L-CT potently slows barbed-end elongation (K_{app} = 0.023 $\pm$ 0.005 nM; Figure 2C,D). Barbed-end binding by FHOD3S-CT is over 30 times weaker (K_{app} = 0.750 $\pm$ 0.090 nM) (Figure 2D, Figure 2—figure supplement 2B). The IA mutation is generally thought to disrupt binding to both actin monomers and filament barbed ends. However, FHOD3L-CT I1163A has an affinity of 4.9 $\pm$ 1.4 nM for barbed ends of actin filaments (Figure 2D). While the affinity is >200-fold weaker than FHOD3L-CT, it still binds barbed ends tightly. Therefore, we interpret the plateau decrease observed in bulk assembly assays as evidence of barbed-end capping.

To directly observe the impact of FHOD3L-CT on growing actin filaments, we used Total Internal Reflection Fluorescence (TIRF) microscopy in the presence of profilin. Most of the filaments elongated at rates indistinguishable from actin alone. Initially, we could not confirm that FHOD3L-CT was bound to these filaments. We, therefore, repeated bulk seeded-elongation assays in the presence of profilin. Under these conditions, we observed increased rates of actin assembly at low doses of FHOD3L-CT, confirming that the formin accelerates elongation (Figure 2E). In contrast, at higher formin concentrations, we found that elongation was actually slower than actin alone. We attribute the complicated shapes and dose response of these data to the contributions of both elongation and capping activities. We also note that the concentrations required for FHOD3L-CT to elicit measurable changes in actin assembly indicate a marked apparent decrease (500-1000 fold) in affinity for the barbed-end when profilin is present (Figure 2E).

Upon closer observation of individual filaments in the TIRF assay, we detected brief pauses followed by short “bursts” of fast elongation (Figure 2F,G, Figure 2—figure supplement 1C). A pause lasted ~12 s on average (Figure 2—figure supplement 1D). During the following bursts, the filaments were dimmer and elongated ~3-fold faster (39 $\pm$ 13 subunits/s), consistent with formin-mediated elongation (Figure 2F,G, Video 1). The average length of filament produced during these bursts was 1.10 $\pm$ 0.49 μm (Figure 2—figure supplement 1E), which is similar to the characteristic run length of *Drosophila* Fhod-A (~2 μm), but very different from other formins, which often range from 20 – 200 μm (Bremer et al., 2024; Cao et al., 2018; Moseley and Goode, 2005; Patel et al., 2018; Vizcarra et al., 2014). FHOD3S-CT mediated similar behavior with indistinguishable pauses, though with slightly, albeit statistically significantly, shorter bursts (characteristic run length of 0.90 $\pm$ 0.33 μm) (Figure 2—figure supplement 2C-E). Thus, for brief intervals, FHOD3S/L-CT caps barbed-ends followed by accelerated elongation, when profilin is present.

Next, we investigated bundling by FHOD3L-CT. To do so, we visually examined the organization of phalloidin-stabilized actin filaments after incubating with FHOD3L-CT. Bundles were readily apparent (Figure 2—figure supplement 1F). To better characterize bundling

activity, we performed low-speed bundling assays with a fixed concentration of actin filaments and several concentrations of FHOD3L-CT (Figure 2H,I). We also compared this activity to bundling by FHOD3S-CT. We found that FHOD3L-CT bundles somewhat more potently than FHOD3S-CT, which is most apparent at concentrations above 15 nM (Figure 2—figure supplement 2F,G).

Overall, FHOD3S/L-CT nucleates and elongates actin. FHOD3S-CT is a more potent nucleator, a weaker barbed-end capper, and a slightly weaker bundler compared to FHOD3L-CT (Table 1). These data suggest that the acidic $T(D/E)_5XE$ insertion of FHOD3L interacts with different surfaces of actin depending on the biochemical activity. Perhaps the marked increase in capping by FHOD3L-CT is mediated by binding to an exposed basic region on the filament. Decreased activity levels of FHOD3L-CT, such as nucleation and bundling, may be due to the fact that most of the actin monomer surface is acidic.

Video 1. TIRF elongation assay. This video shows elongation assays of actin alone and in the presence of 100 pM pHOD3L-CT. Events – pauses before bursts of acceleration – are indicated with arrows in the last movie. (Conditions as in Fig. 2F.)

Biochemical validation of function-separating mutants

We next designed FHOD3L-CT mutants to separate nucleation and elongation. We also assessed the impact of these mutations on capping and bundling. Previously, Baker et al. identified mutations in the FH2 domain of Bni1 that diminish nucleation while maintaining elongation activity (Baker et al., 2015). Based on sequence and structural alignments, FHOD3L K1193 approximates one of these, Bni1 K1467. FHOD3L-CT K1193L nucleated with less than 30% of the strength seen for wild-type (Figure 3A). The barbed-end affinity of FHOD3L-CT K1193L was 0.470 $\pm$ 0.090 nM, ~12-fold weaker than wild-type (Figure 3B). Importantly, K1193L-mediated elongation of actin filaments was indistinguishable from wild-type (no significant difference in elongation rate, run length, or capping duration) (Figure 3C, Figure 3—figure supplement 1A,B). Low-speed bundling assays showed that K1193L bundling is >2-fold weaker than wild-type (Figure 3D). In summary, elongation activity is maintained while nucleation and bundling are strongly reduced by the K1193L mutation.

To remove FH1-mediated acceleration of elongation, we substituted glycine-serine linkers for the polyproline tracts in FHOD3L-CT (Zweifel and Courtemanche, 2020). (The FH2 domain alone was unstable *in vitro*.) Pyrene-based actin assembly assays were confounded by bundling/aggregation induced by this construct. Although low-speed cosedimentation assays indicated that the bundling strength of FHOD3L-CT GS-FH1 is slightly weaker than that of wild-type, images show irregular shapes that may scatter light more, thereby disrupting the pyrene signal (Figure 3D, Figure 3—figure supplement 1C). Therefore, to compare the nucleation strength of FHOD3L-CT GS-FH1 with wildtype, we counted filaments using TIRF microscopy. We observed similar numbers of filaments generated in the presence of low concentrations (used to minimize bundling) of FHOD3L-CT wild-type or GS-FH1 (Figure 3E, Figure 3—figure supplement 1D). Barbed-end elongation assays in the absence of profilin demonstrated a weakened affinity of FHOD3L-CT GS-FH1 (K_{app} = 0.218 $\pm$ 0.016 nM) (Figure 3B). This finding suggests that increasing the stiffness of the FH1 domain impacts barbed end binding but we cannot say whether the effect is direct or indirect. Interestingly, profilin did not decrease barbed-end binding of FHOD3L-CT GS-FH1 (K_{app} = 0.21 $\pm$ 0.13 nM; Figure 3F). Finally, and most importantly deceleration was observed at all concentrations tested in assays with profilin, confirming that elongation is not enhanced by FHOD3L-CT GS-FH1 (Figure 3F). Thus, nucleation is maintained while acceleration of elongation is no longer detected.

Together, these mutations resulted in a range of nucleation, elongation, capping, and bundling activities (Table 1). We, therefore, used them to assess the correlation of biochemical activities with sarcomere formation and function in cardiomyocytes.

FHOD3L rescues sarcomere organization and contractility in neonatal rat ventricular myocytes

In order to perform structure-function analysis in a cellular context, we established methods to knock down and rescue FHOD3L in neonatal rat ventricular myocytes (NRVMs) (similar to (Taniguchi et al., 2009). Briefly, freshly isolated NRVMs were treated with small interfering RNA (siRNA) targeting FHOD3 using reverse transfection (Figure 4A; see Methods for details). Adenoviral infection, driving expression of rescue constructs, was initiated two days after siRNA treatment and cells were examined (fixed or live) two days after infection (Figure 4A). The rescue constructs contained human FHOD3L, which is not targeted by the siRNA used to remove endogenous rat FHOD3. In all cases, cells were treated with siRNA and adenovirus. For negative controls, AllStars Negative Control siRNA and/or empty virus were substituted for the FHOD3-specific reagents. Thus, we refer to the negative control experiment as a mock knockdown and the knockdown alone as a mock rescue. During assay development, we found that knockdown reduced FHOD3 mRNA to ~35% of original levels after four days, with either of two commercially available oligos (Figure 4—figure supplement 1A). At this timepoint, we detected an ~80% reduction in endogenous FHOD3 protein via Western blot (Figure 4B,C).

We analyzed sarcomere structure in fixed samples. To detect sarcomeres, we stained cells with anti-α-actinin antibodies (Figure 4D). To analyze on a per cell basis, we stained plasma membranes with WGA (wheat germ agglutinin) and segmented the NRVMs with CellPose (Figure 4—figure supplement 1B) (Stringer et al., 2021). The DsRed reporter was not an accurate readout of exogenous 3xHA-FHOD3L (hereafter, FHOD3L) expression levels (Figure 4—figure supplement 1C). Therefore, we used anti-HA antibodies to visualize and quantify the expression of exogenous FHOD3 on a per cell basis (Figure 4D, Figure 4—figure supplement 4G). We found that exogenous FHOD3L expression was ~90% above endogenous levels at the end of the rescue timeline (Figure 4B,C). We, therefore, examined the impact of FHOD3L expression level on sarcomere structure. We detected essentially no correlation (R-squared ranges from 0.01 to 0.16) of sarcomere number, length, or width over a three-fold change in FHOD3L expression levels (Figure 4—figure supplement 1D-F). The average HA intensity was within this range for all experiments. Despite the evidence that sarcomere structure was not a function of FHOD3 expression levels, we decided to exclude NRVMs that express very highly above endogenous FHOD3 levels. We set an upper cutoff for the normalized exogenous FHOD3L expression per cell area of 5% and applied that same intensity level as a cutoff for all other experiments (Figure 4—figure supplement 1G). We also set a lower cutoff slightly above background HA levels to exclude NRVMs not expressing exogenous FHOD3L.

We confirmed that sarcomeres remained organized upon mock knockdown, counting 12 $\pm$ 13 sarcomeres per cell (Figure 4D,E, Table 2). (Measurements from NRVMs are summarized in Table 2.) Sarcomeres were largely absent in the mock rescue (3 $\pm$ 7) with α-actinin puncta and aggregates visible by immunofluorescence (IF) (Figure 4D,E). Expression of wild-type FHOD3L was sufficient to rescue the loss of sarcomeres and anti-HA staining demonstrated that exogenous FHOD3L localized to sarcomeres, as expected (Figure 4D). In fact, FHOD3L-rescued NRVMs formed significantly more sarcomeres than the mock knockdown NRVMs (19 $\pm$ 14 vs. 12 $\pm$ 13; Figure 4E). We note that the sarcomere number measurement has a high standard deviation because even within the expression level cutoffs, some cells lacked

sarcomeres. Such right-tailed distributions are consistent with other reports of sarcomere numbers per cardiomyocyte (Neininger-Castro et al., 2023).

To analyze sarcomere integrity more closely, we measured sarcomere lengths (Z-line to Z-line) and widths (Z-line lengths). In the mock rescue cells, the sarcomeres that remained were both shorter and narrower than those in the mock knockdown cells (Figure 4F, G). When rescued with FHOD3L, sarcomere lengths (1.72 $\pm$ 0.18 µm) and sarcomere widths (1.70 $\pm$ 0.46 µm) recovered to lengths comparable to the mock knockdown control (Figure 4F, G). To measure thin filament length, we stained NRVMs with phalloidin and anti-HA (Figure 4 H). We observed shorter thin filament lengths in FHOD3L-rescued NRVMs (739 $\pm$ 81 nm) compared to mock knockdown NRVMs (925 $\pm$ 94 nm) (Figure 4I). The difference in thin filament length could reflect the increased number of sarcomeres in the rescued cells and/or indicate that the sarcomeres have not reached their final steady state after two days of FHOD3L expression. Therefore, FHOD3L-rescued NRVMs form sarcomeres *de novo* that well approximate the sarcomeres in the negative control. We compared further experimental results to FHOD3L rescue cells, due to the slight differences.

We next measured contractile function in FHOD3L-rescued NRVMs. To do so, we used the motionGUI MatLab program that makes use of Digital Image Correlation (DIC) to measure contractility (Huebsch et al., 2015; Nakano et al., 2017). Contraction and relaxation velocities inform us about systolic and diastolic function of the cardiomyocytes, respectively, and thus their ability to promote proper blood flow in organisms (Ferreira-Martins and Leite-Moreira, 2010). As expected, maximal contraction and relaxation velocities were both significantly decreased upon FHOD3 knockdown (Figure 5A,B,D, Figure 5—figure supplement 1A). Both velocities recovered to mock knockdown levels by subsequent expression of FHOD3L (Figure 5A,C,D, Figure 5—figure supplement 1A, Video 2). We also examined expression of FHOD3L in an otherwise untreated background (overexpression). Intensity of exogenous FHOD3L per NRVM was notably lower compared to the wild-type rescue despite infecting with the same titer, suggesting that excel FHOD3L is deleterious and NRVMs attempt to maintain FHOD3L levels below some maximum (Figure 5—figure supplement 2A). Consistent with this idea, contraction and relaxation velocities were reduced upon overexpression of FHOD3L (Figure 5—figure supplement 2B,C). These data further confirm that the expression levels in our rescue experiments, while somewhat higher than endogenous levels, are within an acceptable range.

To assess the impact of FHOD3L depletion on cardiac rhythm, we measured the percentage of beating area in each video that exhibited consistent, rhythmic contractions (defined as no more than 1 beat out of sync in a 10 second period). We observed rhythmic contractions for both the mock knockdown NRVMs and FHOD3L-rescued NRVMs for ~75% of the analyzed videos (Figure 5A,C,E, Video 2). In contrast, primarily arrhythmic contractions were detected in FHOD3-depleted NRVMs, with only ~15% of the videos showing rhythmic beating (Figure 5B,E, Video 2). To assess whether some NRVMs in these conditions were not contracting at all, we estimated the proportion of NRVMs that were contracting per video and found contractions throughout ~95% of the field of view on average for both mock knockdown NRVMs and wild-type FHOD3L-rescued NRVMs (Figure 5—figure supplement 1B). For FHOD3-depleted NRVMs, we observed a reduction in contractile area to ~80% (Figure 5—figure supplement 1B). This value was higher than expected based on other metrics (Figure 5D,E). We attribute much of the movement to neighboring cells pulling each other. We also quantified contractility when we overexpressed FHOD3L. FHOD3L overexpression did not clearly impact the average amount of rhythmic contractions or the area of contraction though variance was increased (Figure 5—figure supplement 2D,E), consistent with the idea that, at high enough levels, FHOD3L activity can be detrimental in NRVMs.

Video 2. Exogenous FHOD3L expression rescues rhythmic contractions in NRVMs. This video shows live NRVMs from control and rescue conditions as in Fig. 5. DIC analysis is indicated by overlaid red and green vectors.

Loss of nucleation but not elongation is tolerated for sarcomere formation and cardiac function

Once we established baseline levels of sarcomere structure and contractility in NRVMs with the wild type FHOD3L rescue, we asked which of FHOD3L's actin organizing activities are important for its cellular function. To this end, we performed rescue experiments with the nucleation-hindering mutant (K1193L) and the elongation-hindering mutant (GS-FH1). Expression of the K1193L mutant resulted in expression levels similar to wild type (Figure 6—figure supplement 1A). Overall, cells expressing FHOD3L K1193L were almost indistinguishable from those expressing FHOD3L. FHOD3L K1193L localization was striated (Figure 6A) and the number of sarcomeres per NRVM was rescued to wild-type levels (15 $\pm$ 16) (Figure 6B). Sarcomere lengths and widths were indistinguishable from wild-type (Figure 6C,D). The only difference was thin filament lengths, which were significantly longer in the K1193L-rescued NRVMs (792 $\pm$ 79 nm) compared to those in FHOD3L-rescued NRVMs (739 $\pm$ 81) (Figure 6E, Figure 6—figure supplement 1B). In agreement with the well-organized, near wild-type appearance of sarcomeres, contraction and relaxation velocities, as well as the proportion of rhythmically contracting NRVMs, were indistinguishable from the FHOD3L rescue (Figure 6F,G, Figure 6—figure supplement 1C,D, Video 3). Thus, ~70% lower nucleation activity, ~20-fold weaker barbed-end capping, and loss of over 50% of bundling activity had no deleterious impact on FHOD3L's ability to function in NRVMs.

In contrast, the elongation deficient mutant (GS-FH1) did not rescue FHOD3L loss in NRVMs. Based on total fluorescence per cell, we determined that GS-FH1 levels were lower than observed for wild-type or K1193L, despite infecting a similar proportion of NRVMs (Figure 6—figure supplement 1A). In a few cells that possibly escaped from RNAi knockdown, we observed a striated pattern of GS-FH1, demonstrating that the protein can fold and localize correctly if sarcomeres are intact (Figure 6—figure supplement 1E). The turnover rate of GS-FH1 may be higher than wild-type intrinsically or because there are few binding sites available. The sarcomere number per cell was only 2 $\pm$ 4, similar to the mock rescue (Figure 6A and B). Within the sarcomeres detected, sarcomere lengths and widths were both reduced (Figure 6C and D). We were not able to measure thin filament lengths with confidence, due to the lack of sarcomere organization. Not surprisingly, contractility was nearly abolished after rescuing with GS-FH1 (Figure 6F,G,Figure 6—figure supplement 1C,D, Video 3). Contraction and relaxation velocities were decreased, and contractions were largely arrhythmic (Figure 6F,G, Figure 6—figure supplement 1C,D). We note that barbed-end capping and bundling activities were weaker than wild-type in the GS-FH1 mutant but they were equivalent or greater than the activities found for the K1193L mutant which rescued well (Figure 3B,D). Therefore, we conclude that elongation activity of FHOD3L is the primary activity required for sarcomere formation, whereas reduced nucleation, barbed-end binding, and bundling activities are well tolerated.

Video 3. Expression of FHOD3L function separating mutants in NRVMs. This video shows live NRVMs from rescues with wild type and function separating mutants, corresponding to Fig 6. Two movies for GS-FH1 reflect the range of contractions we observed with this rescue. DIC analysis is indicated by overlaid red and green vectors.

Discussion

FHOD3L elongation is necessary for sarcomeres in NRVMs

Published rates of nucleation and elongation by formins both range over at least an order of magnitude. It is generally thought that the specific actin assembly properties of a given formin are set for its function, i.e., the structure this formin will build. To directly test this idea, Homa et al. replaced Cdc12p, the formin critical to *S. pombe* cytokinesis, with several chimeras of differing nucleation strength (Homa et al., 2021). Indeed, they found a strong positive correlation between formins with nucleation strength similar to Cdc12p and their ability to drive cytokinesis. In a computational model that recapitulates yeast cable structure, it was found that nucleation and/or elongation could be tuned to build the cables (McInally et al., 2021). Thus, how formins are used is likely to differ from case to case.

Here we determined that FHOD3L can nucleate *in vitro*, albeit weakly compared to many formins. Unlike in cytokinesis, we found that this activity is not necessary for its function in NRVMs. The necessity of actin assembly, nucleation and/or elongation, by Fhod-family formins has been assumed based on failure of the IA mutation to rescue in multiple species (Kan-O et al., 2012; Kimmich et al., 2024; Kutscheidt et al., 2014; Shwartz et al., 2016; Taniguchi et al., 2009). To assess nucleation more specifically, we tested a mutant variant that substantially reduces the nucleation activity without altering elongation (FHOD3L K1193L). This mutant had almost no impact on sarcomere formation or function in NRVMs. The only statistically significant difference we detected was in thin filament length (Figure 6E). A host of proteins are critical to establishing and maintaining thin filaments at a precise length (Szikora et al., 2022). No other studies have implicated FHOD3L in this process to date. Thus, we believe that the length difference is more likely to reflect the state of maturity of the cells (time post infection) and/or the number of sarcomeres per cell. While we only have three data points at this time, sarcomere number and thin filament length were highly correlated (inversely) in our experiments, with an R-squared of 0.90.

By rescuing NRVMs with FHOD3L K1193L, we also tested a formin that caps barbed ends with a K_d that is ~15 times higher than wild type (i.e., ~15x weaker) and bundles filaments ~50% less potently than wild type. The fact that the cardiomyocytes were indistinguishable from wild-type when expressing this mutant suggests that neither of these activities are required and, certainly, they are not needed at wild-type levels. Assuming that FHOD3L activities are tuned to meet its *in vivo* functions, these magnitudes of change in activity would be expected to result in measurable phenotypes in function and/or morphology of the cell.

The fact that K1193L had no impact on the elongation properties of FHOD3L *in vitro* and still rescues sarcomeres leads to an indirect conclusion that elongation is the actin assembly activity that is important in NRVMs. Of course, the failure to rescue by FHOD3L GS-FH1, an elongation incompetent mutant, strongly supports this conclusion (Figure 6). The elongation properties of FHOD3L are unusual. Its elongation rate is among the highest known, including mDia1 and Cappuccino (Bor et al., 2012; Kovar et al., 2006). However, processivity is very brief, resulting in filaments of only ~1 μm. We previously found that the *Drosophila* splice variant FhodA has a similarly short characteristic run length (Patel et al., 2018). In principle, this characteristic run length is sufficient to build sarcomeric thin filaments, which are about 1 μm long in NRVMs. Notably, a splice variant of *Drosophila* Fhod that only differs by having a shorter tail, FhodB, typically elongates for ~20 μm and the tails of mammalian and *Drosophila* formins are highly conserved (Bremer et al., 2024). These observations lead us to question whether processivity of Fhod-family formins is somehow regulated *in vivo* such that it can build short filaments when needed and longer filaments in other contexts. Interestingly, a computational model describing Bni1-built actin cables demonstrates that tuning the length of individual

filaments to cell size is sufficient to account for cable differences in cells of different sizes (McInally et al., 2024).

The FH1 domain strongly influences elongation rate *in vitro*. In NRVMs, we found that replacement of the FH1 domain with a flexible linker (FHOD3L GS-FH1) resulted in a severe phenotype. These cells had very few sarcomeres. FHOD3L GS-FH1 was indistinguishable from mock rescue in sarcomere number, structure (shorter and narrower), and function (contraction and relaxation velocities did not differ). The result could be questioned because the expression levels were lower than those for the other constructs. We argue against this based on two observations: First, despite similar metrics in sarcomere structure and function, the rhythmicity of contraction was markedly diminished, even compared to the mock rescue (Figure 6G). Second, we do not believe that the low protein levels reflect protein instability. We detect FHOD3L GS-FH1 bound to residual sarcomeres, suggesting that it folds and is stable when binding sites within sarcomeres are available (Figure 6—figure supplement 1E). Therefore, we suspect that low FHOD3L GS-FH1 levels reflect the absence of sarcomeres.

Recent work in C. elegans is consistent with our finding. Kimmich et al. removed the endogenous coding region of the FH1 domain in worm Fhod-1 (the only worm Fhod gene) (Kimmich et al., 2024). Body wall muscle is severely impacted by this deletion. In addition, they found that profilin is required for Fhod-1 function. Together these data strongly argue that elongation is important. Interestingly, the muscle phenotype is more severe in a strain that lacks the FH2 domain and all of the upstream sequence but not the FH1 domain. Thus, nucleation activity seems to be necessary in this animal. Ultimately, complete removal of a domain, such as the GS-FH1 mutant is an important starting point but a blunt tool. Future experiments with modified elongation (e.g. slower, more processive) will provide further insight into the biochemical role of FHOD3.

Why does FHOD3L elongate in NRVMs?

Given these new data, what could FHOD3L be doing in the cell? In multiple species, premyofibrils are built but they fail to mature into wild-type myofibrils in the absence of FHOD (Fenix et al., 2018; Kan-O et al., 2012; Kimmich et al., 2024; Shwartz et al., 2016). It follows that FHOD3 is not required to build the earliest thin filaments in the sarcomere. Instead, FHOD3 could contribute new thin filaments to expanding, maturing sarcomeres. If this were the case, we might expect nucleation to be more important than our data indicate. Instead, FHOD3L could be responsible for elongating filaments that are nucleated by a different protein. For example, FHOD3L and DAAM could collaborate, or they could contribute to the apparent redundancy and robustness built in to sarcomerogenesis (Szikora et al., 2022). DAAM knockout mice have overlapping cardiac phenotypes with those of the FHOD3 knockout (Kan-O et al., 2012; Li et al., 2011). Furthermore, a lack of sarcomere thickening and loss of sarcomere organization are common phenotypes in *Drosophila* knockdowns of Daam1 and Fhod (Molnár et al., 2014; Shwartz et al., 2016). While FHOD3L and DAAM cannot compensate for the loss of one or the other, they might work together and be able to help each other when one is compromised.

Alternatively, FHOD3L could be reinforcing the Z-line structure to facilitate sarcomere thickening. This idea is consistent with the narrow myofibrils and Z-body disorder observed in worms lacking functional Fhod-1 (Kimmich et al., 2024; Mi-Mi et al., 2012). However, if capping and bundling were important to the Z-line integrity, one would expect to find FHOD3L localized in the Z-line. In mouse heart tissue, FHOD3L appears to bind directly to MyBP-C which localizes between the Z- and M-lines (Matsuyama et al., 2018b), suggesting that it is not actively stabilizing the Z-line. FHOD localization varies between species and with development,

suggesting that this role is not conserved, if it exists. If, instead, transient actin assembly were sufficient for Z-line stabilization, this role would be consistent with our findings that capping and bundling are not essential in NRVMs.

Materials and Methods

Protein expression, purification, and labeling

FHOD3L-CT (residues 963-1622) was cloned into pGEX-6P-2 with an N-terminal glutathione-S-transferase (GST) tag. The original template, EGFP-Fhod3L, was generously provided by T. Iskratsch (Queen Mary University of London) (Iskratsch et al., 2010). Point mutations were generated by site-directed mutagenesis. Truncations were constructed using FastCloning (Liu and Naismith, 2008). pGEX-FHOD3L-CT GS-FH1, in which the polyproline tracts were replaced with GS linkers was cloned via Gibson Assembly introducing a gBlock into pGEX-FHOD3L-CT (not including the FH1 region).

The FHOD3L-CT wild-type and mutant constructs were transformed in Rosetta 2 (*E. coli* DE3) cells (Novagen), which were grown in 1 liter of Terrific Broth supplemented with 100 mg/liter ampicillin and 32 mg/liter chloramphenicol. Expression was induced at an OD of 0.6-0.8 by adding 0.5 mM isopropyl β-D-1-thiogalacto-pyranoside (IPTG) and shaking overnight at 18°C, 210 rpm. The cells were harvested by centrifugation, washed in PBS, and flash frozen in liquid nitrogen.

Cell pellets expressing GST-FHOD3L-CT wild-type and mutants were resuspended in 20 mM HEPES pH 7.5, 150 mM NaCl, 1 mM PMSF, 1 mM DTT, 2 µg/mL DNaseI. All subsequent steps were performed on ice or at 4°C. The cells were lysed with a microfluidizer, cleared by centrifugation at 20,000 x g for 20 minutes, and then purified using a HitrapSP-FF cation exchange column (GE Life Sciences) with a gradient of 0.2 –0.6 M NaCl over 1 column volume after a 1 column volume wash with 0.2 M NaCl. Peak fractions were dialyzed overnight into 20 mM HEPES pH 8, 200 mM NaCl, 1 mM DTT and Prescission Protease was added to cleave off the GST-tag. This sample was centrifuged at 4°C for 48,000 rpm for 20 minutes, and further purified on a MonoS cation exchange column (GE Life Sciences) with a gradient of 0.2–0.95 M NaCl over 40 column volumes after a 1 column volume wash with 0.2 M NaCl. Peak fractions were exchanged into storage buffer (10 mM Tris pH 8, 150 mM NaCl, 20% glycerol, 1 mM DTT), then flash frozen in liquid nitrogen and stored at -80°C.

Cell pellets expressing GST-FHOD3S-CT were purified and stored similarly to GST-FHOD3L-CT wild-type, except 150 mM NaCl was used throughout the purification with a gradient of 0.15–0.95 M NaCl over 40 column volumes after a 1 column volume wash with 0.15 M NaCl on the MonoS cation exchange column (GE Life Sciences).

Concentrations of C-terminal FHOD3 constructs were determined by running a series of serial dilutions on a Sypro Red-stained quantitative gel using densitometry (ImageJ) with rabbit skeletal actin as the standard. All FHOD3L-CT concentrations are reported as dimer concentrations.

Human Profilin-1 and *Schizosaccharomyces pombe* profilin were expressed and purified as described for *Drosophila* profilin (Chic) (Bor et al., 2012). Profilin-1 concentration was determined using the extinction coefficient 14,992 M^{-1} cm^{-1}. *S. pombe* profilin concentration was determined using 1.63 OD/mg/ml.(Lu and Pollard, 2001)

We used rabbit skeletal muscle actin (RSA) throughout the paper, based on FHOD3L's role in skeletal and cardiac muscle. Skeletal muscle actin was isolated from rabbit back muscle acetone powder (Pel-Freez) according to the method described by Spudich and Watt followed by gel purification (Spudich and Watt, 1971). Skeletal muscle actin was labeled with pyrene iodoacetamide (Thermo Scientific) or Alexa Fluor 488 NHS-ester (Thermo Scientific) as described (Sun et al., 2018).

Pyrene Assays

Pyrene assays were performed essentially as described (Bor et al., 2012) on an Infinite 200 Pro plate reader (Tecan). FHOD3L-CT was diluted in buffer Z (2 mM Tris pH 8.0, 0.2 mM ATP, 0.1 mM $CaCl_2$, 0.5 mM TCEP, 0.04% sodium azide) before addition to polymerization buffer (KMEH: 10mM HEPES, pH 7, 1mM EGTA, 50 mM KCl, 1 mM $MgCl_2$). This mix was added to Mg^{2+}-actin at a final concentration of 4 μM with 5% pyrene-labeled actin. For bulk assembly assays, nucleation strengths were calculated from the slope at $t_{1/8}$ through the origin. The concentration of barbed ends was calculated from the slope (obtained by linear regression over 90 s) as described in (Pollard, 1986 and Patel et al., 2018). For seeded elongation assays, actin filaments were sheared by passing three times through a 24-gauge needle and then aliquoted into each well of a microplate. Proteins were added to the seeds and incubated for 2–4 min at room temperature. Seeds and additional proteins in KMEH were added to Mg^{2+}-actin, at a final concentration of 0.5 μM actin with 10% pyrene-labeled actin, to initiate elongation. Elongation rates were determined by linear regression over the first 90 s and normalized against the rate of actin alone in each experiment. The affinity of FHOD3-CT for barbed ends was determined by fitting the data to the quadratic binding equation:

$$r = a + \mathrm{b} * (([\text{barbed ends}] + [\text{FHOD3} - \text{CT}] + K_d) - \sqrt{([\text{barbed ends}] + [\text{FHOD3} - \text{CT}] + K_d)^2 - 4 * [\text{barbed ends}] * [\text{FHOD3} - \text{CT}]}),$$

where *r* is the normalized elongation rate and *a* and *b* are offset and scaling constants.

Low Speed Bundling Assays

10 μM actin was polymerized for 1 hour at room temperature and diluted to 5 μM with varying amounts of FHOD3-CT constructs in KMEH. Samples were incubated for 30 minutes at room temperature and then spun for 20 min., 14,000 x g to separate the pellet and supernatant. The supernatant samples were carefully transferred to new tubes and the pellet samples were resuspended in an equal volume of 1X sample loading buffer for quantitative comparison. Samples were boiled in 1X sample loading buffer for 10 minutes and run on 10% SDS-PAGE gels. The percentage of actin pelleted was determined via densitometry with FIJI (Schindelin et al., 2012).

TIRF Microscopy

TIRF microscopy was utilized to measure the elongation rates and run lengths of the FHOD3-CT constructs. Coverslips were rinsed three times in MilliQ water, placed in 2% Hellmanex (Hellma Analytics) at 60–65 °C for 2 h, and rinsed another five times in MilliQ water and allowed to dry.

Parallel flow chambers of ~15 μl were assembled on the slide using strips of double-sided tape. Flow chambers were prepared with the following steps: 1) 20 μl of high-salt buffer (50 mM Tris pH 7.5, 600 mM NaCl) for 2 min; 2) 12.5 μl of 60 nM NEM-myosin (stock in 10 mM HEPES pH7, 0.5 M KCl, 10 mM EDTA pH 7.0, 1 mM DTT, 50% glycerol, diluted in high-salt buffer); 3) 20 μl of high-salt BSA-containing buffer (1% BSA, 50 mM Tris pH 7.5, 600 mM NaCl); 4) 20 μl of low-salt BSA-containing buffer (1% BSA, 50 mM Tris pH 7.5, 150 mM NaCl). 5) 50 μl of magnesium-actin and additional proteins to be assayed for a final concentration of 1 μM actin (10% Alexa Fluor 488-labeled) and 5 μM human Profilin-1 in 1X TIRF (KMEH, 0.2 mM ATP, 50 mM DTT, 20 mM glucose, 0.5% methylcellulose (4,000 cP)) buffer supplemented with 250 μg/ml glucose oxidase and 50 μg/ml catalase.

The videos and images were acquired using a Zeiss Axio Observer 7 Basic Marianas Microscope with Definite Focus 2 equipped with a 3i Vector TIRF System, an Alpha Plan-Apochromat 63x (1.46 NA) Oil TIRF Objective, and an Andor iXon3 897 512x512 10 MHz EMCCD Camera, using Slidebook 6 software. Experiments were performed at room temperature. Images were captured at 2.5-s intervals for 10 min. Bright and dim filaments were distinguished manually. Filament lengths were quantified with the JFilament plug-in in FIJI (Schindelin et al., 2012; Smith et al., 2010).

Adenoviral generation, purification, and infection

Adenoviruses containing a full-length FHOD3L wild-type construct were generated by transiently transfecting HEK293 cells using the CalPhos Mammalian Transfection Kit (Catalog No. 631312, Takara Bio) with pAdenoX-CMV-3xHA-FHOD3L-CMV-DsRed after digesting with PacI (NEB) in Cutsmart buffer (NEB) for 1 hr at 37 °C. HEK293 cells were cultured in 1X DMEM (Thermo Fisher, Catalog No. 11965092), 10% FBS (Thermo Fisher, Catalog No. 10082147), and 1% penicillin/streptomycin/amphotericin B (Thermo Fisher, Catalog No. 15240096). Cells were lysed 7-10 days later when noticeable cytopathic effect (CPE) was present and centrifuged at 1.5k x g for 5 min., RT.

Additional crude adenovirus encoding full-length FHOD3L was harvested from infected HEK293. Dilutions and subsequent infections were performed in PBS with magnesium chloride and calcium chloride (PBS+/+) (Thermo Fisher, Catalog No. 14040117) for 1 hr at room temperature, rotating the plate every 10-15 minutes. Plaque formation assays were then performed as in (Baer and Kehn-Hall, 2014). Clone variability was assessed by infecting HEK 293 for each adenoviral clone and observing subsequent DsRed expression over time. Optimal adenoviral clones were selected for large-scale purification. HEK293 were infected, then collected 2-3 days later for purification with the Adeno-X Maxi Purification kit (Takara Bio, Catalog No. 631533).

Crude adenoviruses containing pAV-CMV-{3xHA-FHOD3L GS-FH1}:SV40 pA-CMV-mCherry and pAV-CMV-{3xHA-FHOD3L K1193L}:SV40 pA-CMV-mCherry were commercially generated and purchased from VectorBuilder. The amount of crude adenovirus was estimated by infecting HEK293 cells with serially diluted amounts of crude adenovirus. For large scale purification, HEK293 were infected, then collected 2-3 days later for purification with the Adeno-X Maxi Purification kit (Takara Bio, Catalog No. 631533).

Particle titers of purified viruses were quantified by making three separate dilutions of each virus in 0.1% SDS (Thermo Fisher) and vortexing for 5 minutes, spinning down 13,000 x rpm, 5 minutes, and then taking the average of the absorbance readings on the Nanophotometer N50-GO (Implen) to quantify particles/mL as per (Maizel et al., 1968).

Neonatal rat ventricular myocyte seeding, siRNA knockdown, and rescue

The 8-well chamber slides (Corning, Catalog No. 354118) were prepared by coating with 10 μg/mL fibronectin (Sigma, Catalog No. F1141) and 20 μg/mL poly-D-lysine hydrobromide (Sigma, Catalog No. P6407) in PBS overnight at 4°C. Neonatal rat ventricular myocytes (NRVMs) were seeded at 175,000 NRVMs/well in a mixture of 75% DMEM (Thermo Fisher, Catalog No. 11965092), 15% Medium-199 (Thermo Fisher, Catalog No. 11150059) supplemented with 2 mM L-glutamine (Thermo Fisher, Catalog No. A2916801) and 10 mM HEPES (Thermo Fisher, Catalog No. 15630080). For reverse transfection, the cells were treated with siRNA targeting FHOD3 (Qiagen, Rn_LOC100360334_2 Flexitube siRNA) or AllStars Negative Control siRNA (Qiagen, 20 nmol), Lipofectamine RNAiMAX transfection reagent (Thermo Fisher, Catalog No. 13778075) and Opti-MEM I Reduced Serum Medium (Thermo Fisher, Catalog No. 31985062) to dilute the siRNA. Media was changed 24 hours later to one containing penicillin/streptomycin (Thermo Fisher, Catalog No. 15140122). NRVMs were infected with an optimal amount of adenovirus (determined experimentally to be particle titer MOI 350 to minimize excessive damage to NRVMs while maintaining sufficient expression) as above 48 hours after seeding and media containing penicillin/streptomycin was added on top of the PBS+/+ at the end of the infection. Media was changed 24 hours later and cells were examined 48 hours after infection.

Gene expression analysis by quantitative reverse-transcriptase PCR

RNA was extracted from the NRVMs four days after reverse transfection of siRNA using the Direct-zol RNA mini prep kit (Zymo Research, Catalog No. R2050). RNA was reverse-transcribed into complementary DNA using the qScript cDNA synthesis kit (Quanta Biosciences, Catalog No. 95047-025). Quantitative reverse-transcriptase PCR was performed using PowerUp SYBR green master mix for qPCR (Applied Biosystems, Catalog No. A25742) on a Lightcycler 480 (Roche). Each qPCR reaction was repeated three times. Forward and reverse primer sequences are as follows: GAPDH forward, CCGCATCTTCTTGTGCAGTG; GAPDH reverse, CGATACGGCCAAATCCGTTC; FHOD3 forward, CAGCCAATCACGGAG; FHOD3 reverse, TGCTGTCCTTGCCCTGA.

Western blots

NRVMs were lysed in 100 mM Tris pH 8, 150 mM NaCl, 0.5% Triton-X from 8-well chamber slides (Corning, Catalog No. 354118) after rescue experiments and samples were vortexed for 1 minute before centrifuging at 15,000 rpm, 4°C, for 10 minutes. The resulting supernatant was boiled in sample loading buffer at 100°C for 10 minutes and run on an SDS-PAGE gel. The gel was transferred to an Immobilon-FL polyvinylidene fluoride membrane (Millipore, IPFL00010) at 100V for 90 minutes on ice. The membrane was blocked in 4% nonfat milk in low-salt TBST (20 mM Tris pH 7.6, 150 mM NaCl, 0.05% Tween-20, 0.01% sodium azide) for 30 minutes at room temperature. It was incubated, rotating at 4°C overnight, with Fhod3 polyclonal rabbit (Abcam, ab224463) or HA monoclonal rabbit (Cell Signaling

Technologies, 3724S) and GAPDH monoclonal mouse (Santa Cruz Biotechnology, sc-365062) diluted 1:1000 in low-salt TBST. Membranes were washed 3 times for 5 minutes each the next day in high-salt TBST (20 mM Tris pH 7.6, 500 mM NaCl, 0.05% Tween-20, 0.01% sodium azide) and then incubated for 1 hour at room temperature, shaking, with 800CW goat anti-rabbit IgG secondary antibody (Li-Cor Biosciences, 926-32211) and 680RD goat anti-mouse IgG secondary antibody (Li-Cor Biosciences, 926-68070) diluted 1:10,000 in high-salt TBST. Membranes were washed 3 times for 10 minutes each in high-salt TBST and then imaged on a Li-Cor Odyssey 9120 Infrared Imager (Li-Cor Biosciences).

In vitro contractility assay

Contractility assessments were performed by utilizing a video-based technique with the UCSF Gladstone-developed MATLAB program MotionGUI (Huebsch et al., 2015). Videos for contractility analysis were acquired using MicroManager software on a Leica SD AF Spinning Disc system using a HC PL Fluotar 10x (0.3 NA) dry objective lens with an ORCA-Flash4.0 LT C11440 camera (Hamamatsu) at 30 fps with live NRVMs incubated at 37°C, 5% CO_2 (Tokai Hit). The videos were converted from ome.tif to a tiff stack with FIJI for analysis with MotionGUI. A pixel size of 0.538 μm was obtained from the metadata. 8 pixel macroblocks were used for all assessments. All parameters of the MotionGUI program not specified here were set to their respective default values. Motion vectors were calculated, and the data were evaluated upon completion. All videos were subjected to the same post-processing procedures to ensure consistency during comparative analysis. Each video sample was post-processed using neighbor-based cleaning with the vector-based cleaning criterion within the program. The threshold for this post-processing method was set to two for all samples and was adequate for improving the signal-to-noise ratio enough to identify peaks clearly corresponding to beating events in most samples.

Immunofluorescence and image analysis

For sarcomere integrity analysis, NRVMs were stained before fixation with Wheat Germ Agglutinin (WGA) TMR (Thermo Fisher, Catalog No. W849) for 10 minutes at 37°C with 5 μg/mL WGA, followed by two PBS washes. NRVMs were then fixed with 4% paraformaldehyde (Fisher Scientific, Catalog No. AC416780010) in PBS for 15 minutes at 37°C. Cells were washed 3 times in PBS for 5 minutes each at room temperature. Cells were permeabilized and blocked with PBS/0.1% Triton-X/10% Goat Serum (Triton-X: Thermo Fisher, Catalog No. A16046.AP; Goat Serum: Sigma, Catalog No. S26-100ML) for 30 minutes at 37°C. Cells were incubated with primary antibodies overnight at 4°C. α-actinin (mouse) primary antibody (Sigma, Catalog No. A7811) was diluted 1:250 and HA-tag (rabbit) primary antibody (Cell Signaling, Catalog No. 3724) was diluted 1:500 in PBS/0.1% Triton-X/5% Goat Serum. Cells were washed 3 times for 5 minutes each with PBS/0.1% Triton-X/5% Goat Serum at room temperature. Incubation with secondary antibodies was for 1 hour at 37°C. Alexa Fluor 488 goat anti-mouse secondary (Thermo Fisher, Catalog No. A-11001) or Alexa Fluor 647 goat anti-rabbit secondary (Thermo Fisher, Catalog No. A-21244) was diluted 1:500 in PBS/0.1% Triton-X/5% Goat Serum. Cells were then washed twice in PBS/0.1% Triton-X/5% Goat Serum for 5 minutes each followed by on PBS wash for 5 minutes before mounting in Vectashield Plus Antifade mounting media (Vector Laboratories, Catalog No. H-1900-10) with 1 μg/mL DAPI (Fisher Scientific, Catalog No. EN62248).

For thin filament determination, NRVM's were incubated with sterile-filtered Ringer's relaxation buffer (6 mM potassium phosphate pH 7.0, 100 mM NaCl, 2 mM KCl, 0.1% glucose, 2 mM $MgCl_2$, 1 mM EGTA) for 20 min., room temperature, followed by a brief PBS wash to start the WGA staining. Fixation and blocking were performed as above. Staining with HA-tag (rabbit) primary antibody Alexa Fluor 647 goat anti-rabbit secondary antibody were performed as above. Cells were then washed twice in PBS/0.1% Triton-X/5% Goat Serum for 5 minutes each and 200 nM Alexa Fluor 488 phalloidin (Thermo Fisher, Catalog No. A12379) was added for 1 hr, room temperature in PBS/1% BSA. Cells were washed with PBS twice for 5 minutes before mounting in Prolong Glass Antifade mountant (Thermo Fisher, Catalog No. P36980) with 1 μg/mL DAPI (Fisher Scientific, Catalog No. EN62248).

Twelve 40X magnification images per biological replicate were acquired using a random coordinate generator (https://onlineintegertools.com/generate-integer-pairs), excluding the edges of the wells, for quantification of sarcomeres and thin filaments. Sample size with sufficient power was determined via a small-scale pilot study for sarcomere number, length, and width, as well as thin filaments between mock knockdown, mock rescue, and FHOD3L WT rescue followed by inputting averages of the treatments on https://www.stat.ubc.ca/~rollin/stats/ssize/n1.html. Each well was treated as a 16x16 grid of 40X magnification fields of view. 16-bit images were acquired on an AXIO Imager.D1 fluorescence phase contrast microscope (Zeiss) using an EC Plan-Neofluor 40x M27 (0.75 NA) objective lens with an AxioCam MRm camera (Zeiss). Images of NRVMs in figures were acquired with a Plan-Apochromat oil DIC M27 63x (1.4 NA) objective lens for visualization.

Images showing DsRed reporter fluorescence at the end of the rescue timeline for the NRVMs were taken on a CKX53 inverted phase contrast microscope (Olympus) using a UPLFLN 4x (0.2 NA) objective lens (Olympus) with an ORCA-spark digital CMOS camera (Hamamatsu).

Cells were segmented using Cellpose (Stringer et al., 2021). Two-color images of the WGA membrane stain and nuclear stain were saved as jpeg files on FIJI. These images were then input to the Cellpose environment for batch processing with a cell diameter of 210 pixels, 0.4 cell probability and flow thresholds, 0 stitch threshold, using the cyto2 model for segmentation. The text files of the outlines were saved and overlaid on the respective channels of the images individually using the provided python file from Cellpose as a macro through FIJI (imagej_roi_converter.py). Cellpose segments with no nuclei or 3 or more nuclei, as well as cell segments on the edge of the image were excluded from analysis.

Sarcomere analysis was performed manually in a single-blind manner (for mock knockdown, mock rescue, wild-type rescue, and the K1193L rescue) using blindrename.pl (https://github.com/davalencia0914/sarcApp_Cellpose_Merge) to generate the filenames and a key filename csv file for decoding after analysis. We attempted to blind all other rescue conditions, but they were too easily identified based on expression level and localization differences. Linescans were generated along myofibrils, perpendicular to the Z-lines to make sarcomere length measurements from Z-line peak to Z-line peak. Z-line lengths were measured by visual inspection of the alpha-actinin channel and measured on FIJI with the line tool. Three or more consecutive Z-lines at least 0.70 µm long in a row were analyzed as sarcomeres.

Statistical analysis

To compare two or more groups for the rescue experiments in NRVMs, pair-wise comparisons were performed. In order to reduce Type 1 error rate stemming from multiple comparisons, Bonferroni correction was applied to obtain a corrected alpha. Whether groups were normally distributed or not was determined by the Shapiro-Wilk test. To compare two normally distributed groups, Student's two-sample, unpaired t-test was used. If either group was not normally distributed, the non-parametric Mann-Whitney U test was used. The same analysis was applied to analyze run lengths and capping duration from the TIRF seeded elongation assays.

For the nucleation assay, barbed-end binding assays, and TIRF elongation rate analysis, one-way ANOVA's were performed for 3 treatment comparisons with post-hoc Tukey tests as the variances between all treatments tested were fairly equal.

In all cases when the sample size exceeded 20, we removed outliers from the bottom and upper 2.5% of data to perform all statistical tests, regardless of normality, to avoid introducing bias. However, all plots shown include these outliers.

Data Availability

All data described in the manuscript are contained within the manuscript. Additional information and data are available upon request. All code used can be found on Github (https://github.com/davalencia0914/sarcApp_Cellpose_Merge).

Funding and additional information – This work was supported by NIH grant R01 HL146159 to M.E.Q., and Ruth L. Kirschstein National Research Service Award T32 GM007185 to D.A.V. and T32 AR065972 to A.N.K. Confocal laser scanning microscopy was performed at the Advanced Light Microscopy/Spectroscopy Laboratory and Leica Microsystems Center of Excellence at the California NanoSystems Institute at UCLA (RRID:SCR_022789) with funding support from NIH Shared Instrumentation Grant S10OD025017 and NSF Major Research Instrumentation grant CHE-072251.

Author contributions – D. A. V., A. N. K., A. N., and M. E. Q. designed the experiments. D. A. V. and A. N. K. performed the experiments. A. H. and H. N. provided essential experimental support and advice. D. A. V. and A. R. performed the statistical analysis. D. A. V. and C. S. performed manual sarcomere analysis. D. A. V., H. N., A. N., and M. E. Q. wrote the manuscript with input from all authors.

Acknowledgements – We thank members of the Quinlan lab and Nakano lab for experimental support and scientific feedback, the Reisler lab for valuable discussions and reagents, the Courtemanche lab for NEM-myosin, and T. Iskratsch for the FHOD plasmids. We also thank Dr. Michael D. Roth for access to his lab's BSL II-equipped facilities, enabling the production of adenovirus. Neonatal rat ventricular myocytes (NRVMs) were isolated from post-natal P1-P3 day old Sprague-Dawley rat pups of mixed gender by UCLA Cardiovascular Research Theme Core services. We thank Brian Jeong at California NanoSystems Institute at UCLA for assisting us with video imaging for contractility assays.

References

Al Haj A, Mazur AJ, Radaszkiewicz K, Radaszkiewicz T, Makowiecka A, Stopschinski BE, Schönichen A, Geyer M, Mannherz HG. 2015. Distribution of formins in cardiac muscle: FHOD1 is a component of intercalated discs and costameres. *European Journal of Cell Biology* **94**:101–113. doi:10.1016/j.ejcb.2014.11.003

Antoku S, Schwartz TU, Gundersen GG. 2023. FHODs: Nuclear tethered formins for nuclear mechanotransduction. *Frontiers in Cell and Developmental Biology* **11**.

Arimura T, Takeya R, Ishikawa T, Yamano T, Matsuo A, Tatsumi T, Nomura T, Sumimoto H, Kimura A. 2013. Dilated Cardiomyopathy-Associated *FHOD3* Variant Impairs the Ability to Induce Activation of Transcription Factor Serum Response Factor. https://www.jstage.jst.go.jp/article/circj/77/12/77_CJ-13-0255/_article

Baer A, Kehn-Hall K. 2014. Viral Concentration Determination Through Plaque Assays: Using Traditional and Novel Overlay Systems. *J Vis Exp* 52065. doi:10.3791/52065

Baker JL, Courtemanche N, Parton DL, McCullagh M, Pollard TD, Voth GA. 2015. Electrostatic Interactions between the Bni1p Formin FH2 Domain and Actin Influence Actin Filament Nucleation. *Structure* **23**:68–79. doi:10.1016/j.str.2014.10.014

Bechtold M, Schultz J, Bogdan S. 2014. FHOD proteins in actin dynamics—a formin' class of its own. *Small GTPases* **5**:e973765. doi:10.4161/21541248.2014.973765

Blanchoin L, Boujemaa-Paterski R, Sykes C, Plastino J. 2014. Actin Dynamics, Architecture, and Mechanics in Cell Motility. *Physiological Reviews* **94**:235–263. doi:10.1152/physrev.00018.2013

Bor B, Vizcarra CL, Phillips ML, Quinlan ME. 2012. Autoinhibition of the formin Cappuccino in the absence of canonical autoinhibitory domains. *Mol Biol Cell* **23**:3801–3813. doi:10.1091/mbc.E12-04-0288

Boussaty EC, Ninoyu Y, Andrade L, Li Q, Takeya R, Sumimoto H, Ohyama T, Wahlin KJ, Manor U, Friedman RA. 2023. Altered Fhod3 Expression Involved in Progressive High-Frequency Hearing Loss via Dysregulation of Actin Polymerization Stoichiometry in The Cuticular Plate. *bioRxiv* 2023.07.20.549974. doi:10.1101/2023.07.20.549974

Bremer KV, Wu C, Patel AA, He KL, Grunfeld AM, Chanfreau GF, Quinlan ME. 2024. Formin tails act as a switch, inhibiting or enhancing processive actin elongation. *J Biol Chem* **300**:105557. doi:10.1016/j.jbc.2023.105557

Cao L, Kerleau M, Suzuki EL, Wioland H, Jouet S, Guichard B, Lenz M, Romet-Lemonne G, Jegou A. 2018. Modulation of formin processivity by profilin and mechanical tension. *Elife* **7**:e34176. doi:10.7554/eLife.34176

Courtemanche N. 2018. Mechanisms of formin-mediated actin assembly and dynamics. *Biophys Rev* **10**:1553–1569. doi:10.1007/s12551-018-0468-6

Cutler KJ, Stringer C, Wiggins PA, Mougous JD. 2021. Omnipose: a high-precision morphology-independent solution for bacterial cell segmentation (preprint). Microbiology. doi:10.1101/2021.11.03.467199

Deng S, Silimon RL, Balakrishnan M, Bothe I, Juros D, Soffar DB, Baylies MK. 2021. The actin polymerization factor Diaphanous and the actin severing protein Flightless I collaborate to regulate sarcomere size. *Developmental Biology* **469**:12–25. doi:10.1016/j.ydbio.2020.09.014

884 Dominguez R, Holmes KC. 2011. Actin Structure and Function. *Annu Rev Biophys* **40**:169–186.
885 doi:10.1146/annurev-biophys-042910-155359
886 Dwyer J, Pluess M, Iskratsch T, Dos Remedios CG, Ehler E. 2014. The formin FHOD1 in
887 cardiomyocytes. *Anat Rec (Hoboken)* **297**:1560–1570. doi:10.1002/ar.22984
888 Fenix AM, Neininger AC, Taneja N, Hyde K, Visetsouk MR, Garde RJ, Liu B, Nixon BR, Manalo AE,
889 Becker JR, Crawley SW, Bader DM, Tyska MJ, Liu Q, Gutzman JH, Burnette DT. 2018.
890 Muscle-specific stress fibers give rise to sarcomeres in cardiomyocytes. *eLife* **7**:e42144.
891 doi:10.7554/eLife.42144
892 Ferreira-Martins J, Leite-Moreira AF. 2010. Physiologic Basis and Pathophysiologic Implications
893 of the Diastolic Properties of the Cardiac Muscle. *J Biomed Biotechnol* **2010**:807084.
894 doi:10.1155/2010/807084
895 Fujimoto N, Kan-O M, Ushijima T, Kage Y, Tominaga R, Sumimoto H, Takeya R. 2016. Transgenic
896 Expression of the Formin Protein Fhod3 Selectively in the Embryonic Heart: Role of
897 Actin-Binding Activity of Fhod3 and Its Sarcomeric Localization during
898 Myofibrillogenesis. *PLoS ONE* **11**:e0148472. doi:10.1371/journal.pone.0148472
899 Gasteier JE, Madrid R, Krautkrämer E, Schröder S, Muranyi W, Benichou S, Fackler OT. 2003.
900 Activation of the Rac-binding partner FHOD1 induces actin stress fibers via a ROCK-
901 dependent mechanism. *J Biol Chem* **278**:38902–38912. doi:10.1074/jbc.M306229200
902 Goode BL, Eck MJ. 2007. Mechanism and Function of Formins in the Control of Actin Assembly.
903 *Annual Review of Biochemistry* **76**:593–627.
904 doi:10.1146/annurev.biochem.75.103004.142647
905 Homa KE, Zsolnay V, Anderson CA, O'Connell ME, Neidt EM, Voth GA, Bidone TC, Kovar DR.
906 2021. Formin Cdc12's specific actin assembly properties are tailored for cytokinesis in
907 fission yeast. *Biophysical Journal* **120**:2984–2997. doi:10.1016/j.bpj.2021.06.023
908 Huebsch N, Loskill P, Mandegar MA, Marks NC, Sheehan AS, Ma Z, Mathur A, Nguyen TN, Yoo
909 JC, Judge LM, Spencer CI, Chukka AC, Russell CR, So P-L, Conklin BR, Healy KE. 2015.
910 Automated Video-Based Analysis of Contractility and Calcium Flux in Human-Induced
911 Pluripotent Stem Cell-Derived Cardiomyocytes Cultured over Different Spatial Scales.
912 *Tissue Engineering Part C: Methods* **21**:467–479. doi:10.1089/ten.tec.2014.0283
913 Iskratsch T, Lange S, Dwyer J, Kho AL, Remedios C dos, Ehler E. 2010. Formin follows function: a
914 muscle-specific isoform of FHOD3 is regulated by CK2 phosphorylation and promotes
915 myofibril maintenance. *Journal of Cell Biology* **191**:1159–1172.
916 doi:10.1083/jcb.201005060
917 Iskratsch T, Yu C-H, Mathur A, Liu S, Stévenin V, Dwyer J, Hone J, Ehler E, Sheetz M. 2013.
918 FHOD1 Is Needed for Directed Forces and Adhesion Maturation during Cell Spreading
919 and Migration. *Developmental Cell* **27**:545–559. doi:10.1016/j.devcel.2013.11.003
920 Kanaya H, Takeya R, Takeuchi K, Watanabe N, Jing N, Sumimoto H. 2005. Fhos2, a novel formin-
921 related actin-organizing protein, probably associates with the nestin intermediate
922 filament. *Genes to Cells* **10**:665–678. doi:10.1111/j.1365-2443.2005.00867.x
923 Kan-o M, Takeya R, Abe T, Kitajima N, Nishida M, Tominaga R, Kurose H, Sumimoto H. 2012a.
924 Mammalian formin Fhod3 plays an essential role in cardiogenesis by organizing
925 myofibrillogenesis | Biology Open | The Company of Biologists.
926 https://journals.biologists.com/bio/article/1/9/889/19745/Mammalian-formin-Fhod3-
927 plays-an-essential-role-in

928 Kan-O M, Takeya R, Abe T, Kitajima N, Nishida M, Tominaga R, Kurose H, Sumimoto H. 2012.
929 Mammalian formin Fhod3 plays an essential role in cardiogenesis by organizing
930 myofibrillogenesis. *Biology Open* **1**:889–896. doi:10.1242/bio.20121370
931 Kan-o M, Takeya R, Taniguchi K, Tanoue Y, Tominaga R, Sumimoto H. 2012b. Expression and
932 Subcellular Localization of Mammalian Formin Fhod3 in the Embryonic and Adult Heart.
933 *PLOS ONE* **7**:e34765. doi:10.1371/journal.pone.0034765
934 Kimmich MJ, Sundaramurthy S, Geary MA, Lesanpezeshki L, Yingling CV, Vanapalli SA, Littlefield
935 RS, Pruyne D. 2024. FHOD-1/profilin-mediated actin assembly protect sarcomeres
936 against contraction-induced deformation in C. elegans. doi:10.1101/2024.02.29.582848
937 Koka S, Neudauer CL, Li X, Lewis RE, McCarthy JB, Westendorf JJ. 2003. The formin-homology-
938 domain-containing protein FHOD1 enhances cell migration. *Journal of Cell Science*
939 **116**:1745–1755. doi:10.1242/jcs.00386
940 Kovar DR, Harris ES, Mahaffy R, Higgs HN, Pollard TD. 2006. Control of the Assembly of ATP- and
941 ADP-Actin by Formins and Profilin. *Cell* **124**:423–435. doi:10.1016/j.cell.2005.11.038
942 Kutscheidt S, Zhu R, Antoku S, Luxton GWG, Stagljar I, Fackler OT, Gundersen GG. 2014. FHOD1
943 interaction with nesprin-2G mediates TAN line formation and nuclear movement. *Nat*
944 *Cell Biol* **16**:708–715. doi:10.1038/ncb2981
945 Lappalainen P, Kotila T, Jégou A, Romet-Lemonne G. 2022. Biochemical and mechanical
946 regulation of actin dynamics. *Nat Rev Mol Cell Biol* **23**:836–852. doi:10.1038/s41580-
947 022-00508-4
948 Li D, Hallett MA, Zhu W, Rubart M, Liu Y, Yang Z, Chen H, Haneline LS, Chan RJ, Schwartz RJ,
949 Field LJ, Atkinson SJ, Shou W. 2011. Dishevelled-associated activator of morphogenesis 1
950 (Daam1) is required for heart morphogenesis. *Development* **138**:303–315.
951 doi:10.1242/dev.055566
952 Li F, Higgs HN. 2005. Dissecting Requirements for Auto-inhibition of Actin Nucleation by the
953 Formin, mDia1. *J Biol Chem* **280**:6986–6992. doi:10.1074/jbc.M411605200
954 Liu H, Naismith JH. 2008. An efficient one-step site-directed deletion, insertion, single and
955 multiple-site plasmid mutagenesis protocol. *BMC Biotechnol* **8**:91. doi:10.1186/1472-
956 6750-8-91
957 Lu J, Pollard TD. 2001. Profilin Binding to Poly-l-Proline and Actin Monomers along with Ability
958 to Catalyze Actin Nucleotide Exchange Is Required for Viability of Fission Yeast. *Mol Biol*
959 *Cell* **12**:1161–1175. doi:10.1091/mbc.12.4.1161
960 Maizel JV, White DO, Scharff MD. 1968. The polypeptides of adenovirus: I. Evidence for multiple
961 protein components in the virion and a comparison of types 2, 7A, and 12. *Virology*
962 **36**:115–125. doi:10.1016/0042-6822(68)90121-9
963 Matsuyama S, Kage Y, Fujimoto N, Ushijima T, Tsuruda T, Kitamura K, Shiose A, Asada Y,
964 Sumimoto H, Takeya R. 2018a. Interaction between cardiac myosin-binding protein C
965 and formin Fhod3. *Proceedings of the National Academy of Sciences* **115**:E4386–E4395.
966 doi:10.1073/pnas.1716498115
967 Matsuyama S, Kage Y, Fujimoto N, Ushijima T, Tsuruda T, Kitamura K, Shiose A, Asada Y,
968 Sumimoto H, Takeya R. 2018b. Interaction between cardiac myosin-binding protein C
969 and formin Fhod3. *Proceedings of the National Academy of Sciences* **115**:E4386–E4395.
970 doi:10.1073/pnas.1716498115

McInally SG, Kondev J, Goode BL. 2021. Scaling of subcellular actin structures with cell length through decelerated growth. *eLife* **10**:e68424. doi:10.7554/eLife.68424

McInally SG, Reading AJB, Rosario A, Jelenkovic PR, Goode BL, Kondev J. 2024. Length control emerges from cytoskeletal network geometry. *Proceedings of the National Academy of Sciences* **121**:e2401816121. doi:10.1073/pnas.2401816121

Mi-Mi L, Votra S, Kemphues K, Bretscher A, Pruyne D. 2012. Z-line formins promote contractile lattice growth and maintenance in striated muscles of C. elegans. *J Cell Biol* **198**:87–102. doi:10.1083/jcb.201202053

Molnár I, Migh E, Szikora S, Kalmár T, Végh AG, Deák F, Barkó S, Bugyi B, Orfanos Z, Kovács J, Juhász G, Váró G, Nyitrai M, Sparrow J, Mihály J. 2014. DAAM Is Required for Thin Filament Formation and Sarcomerogenesis during Muscle Development in Drosophila. *PLOS Genetics* **10**:e1004166. doi:10.1371/journal.pgen.1004166

Moseley JB, Goode BL. 2005. Differential Activities and Regulation of Saccharomyces cerevisiae Formin Proteins Bni1 and Bnr1 by Bud6. *Journal of Biological Chemistry* **280**:28023–28033. doi:10.1074/jbc.M503094200

Myasnikov R, Bukaeva A, Kulikova O, Meshkov A, Kiseleva A, Ershova A, Petukhova A, Divashuk M, Zotova E, Sotnikova E, Kharlap M, Zharikova A, Vyatkin Y, Ramensky V, Abisheva A, Muraveva A, Koretskiy S, Kudryavtseva M, Popov S, Utkina M, Mershina E, Sinitsyn V, Kogan E, Blagova O, Drapkina O. 2022. A Case of Severe Left-Ventricular Noncompaction Associated with Splicing Altering Variant in the FHOD3 Gene. *Genes* **13**:309. doi:10.3390/genes13020309

Nakano H, Minami I, Braas D, Pappoe H, Wu X, Sagadevan A, Vergnes L, Fu K, Morselli M, Dunham C, Ding X, Stieg AZ, Gimzewski JK, Pellegrini M, Clark PM, Reue K, Lusis AJ, Ribalet B, Kurdistani SK, Christofk H, Nakatsuji N, Nakano A. 2017. Glucose inhibits cardiac muscle maturation through nucleotide biosynthesis. *eLife* **6**:e29330. doi:10.7554/eLife.29330

Neininger-Castro AC, Jr JBH, Sanchez ZC, Taneja N, Fenix AM, Moparthi S, Vassilopoulos S, Burnette DT. 2023. Independent regulation of Z-lines and M-lines during sarcomere assembly in cardiac myocytes revealed by the automatic image analysis software sarcApp. *eLife* **12**. doi:10.7554/eLife.87065.2

Ochoa JP, Sabater-Molina M, Garcia-Pinilla JM, Mogensen J, Restrepo-Cordoba A, Palomino-Doza J, Villacorta E, Martinez-Moreno M, Ramos-Maqueda J, Zorio E, Peña-Peña ML, García-Granja PE, Rodríguez-Palomares JF, Cárdenas-Reyes IJ, de la Torre-Carpente MM, Bautista-Pavés A, Akhtar MM, Cicerchia MN, Bilbao-Quesada R, Mogollón-Jimenez MV, Salazar-Mendiguchía J, Mesa Latorre JM, Arnaez B, Olavarri-Miguel I, Fuentes-Cañamero ME, Lamounier Jr A, Pérez Ruiz JM, Climent-Payá V, Monserrat L. 2018. Formin Homology 2 Domain Containing 3 (FHOD3) Is a Genetic Basis for Hypertrophic Cardiomyopathy - ScienceDirect. https://www.sciencedirect.com/science/article/pii/S073510971838673X?via%3Dihub

Patel AA, Oztug Durer ZA, van Loon AP, Bremer KV, Quinlan ME. 2018. Drosophila and human FHOD family formin proteins nucleate actin filaments. *J Biol Chem* **293**:532–540. doi:10.1074/jbc.M117.800888

1013 Paul A, Pollard T. 2008. The Role of the FH1 Domain and Profilin in Formin-Mediated Actin-
1014 Filament Elongation and Nucleation. *Current Biology* **18**:9–19.
1015 doi:10.1016/j.cub.2007.11.062
1016 Paul AS, Pollard TD. 2009. Review of the mechanism of processive actin filament elongation by
1017 formins. *Cell Motil Cytoskeleton* **66**:606–17. doi:10.1002/cm.20379
1018 Pollard TD. 2016. Actin and Actin-Binding Proteins. *Cold Spring Harb Perspect Biol* a018226.
1019 doi:10.1101/cshperspect.a018226
1020 Rosado M, Barber CF, Berciu C, Feldman S, Birren SJ, Nicastro D, Goode BL. 2014. Critical roles
1021 for multiple formins during cardiac myofibril development and repair. *Mol Biol Cell*
1022 **25**:811–827. doi:10.1091/mbc.E13-08-0443
1023 Sanematsu F, Kanai A, Ushijima T, Shiraishi A, Abe T, Kage Y, Sumimoto H, Takeya R. 2019.
1024 Fhod1, an actin-organizing formin family protein, is dispensable for cardiac development
1025 and function in mice. *Cytoskeleton* cm.21523. doi:10.1002/cm.21523
1026 Sanger JW, Wang J, Fan Y, White J, Mi-Mi L, Dube DK, Sanger JM, Pruyne D. 2017. Assembly and
1027 Maintenance of Myofibrils in Striated Muscle. *Handb Exp Pharmacol* **235**:39–75.
1028 doi:10.1007/164_2016_53
1029 Schindelin J, Arganda-Carreras I, Frise E, Kaynig V, Longair M, Pietzsch T, Preibisch S, Rueden C,
1030 Saalfeld S, Schmid B, Tinevez J-Y, White DJ, Hartenstein V, Eliceiri K, Tomancak P,
1031 Cardona A. 2012. Fiji: an open-source platform for biological-image analysis. *Nat*
1032 *Methods* **9**:676–682. doi:10.1038/nmeth.2019
1033 Schonichen A, Geyer M. 2010. Fifteen formins for an actin filament: a molecular view on the
1034 regulation of human formins. *Biochim Biophys Acta* **1803**:152–63.
1035 doi:10.1016/j.bbamcr.2010.01.014
1036 Schonichen A, Mannherz HG, Behrmann E, Mazur AJ, Kuhn S, Silvan U, Schoenenberger C-A,
1037 Fackler OT, Raunser S, Dehmelt L, Geyer M. 2013. FHOD1 is a combined actin filament
1038 capping and bundling factor that selectively associates with actin arcs and stress fibers.
1039 *Journal of Cell Science* **126**:1891–1901. doi:10.1242/jcs.126706
1040 Schulze N, Graessl M, Soares AB, Geyer M, Dehmelt L, Nalbant P. 2014. FHOD1 regulates stress
1041 fiber organization by controlling the dynamics of transverse arcs and dorsal fibers. *J Cell*
1042 *Sci* **127**:1379–1393. doi:10.1242/jcs.134627
1043 Shwartz A, Dhanyasi N, Schejter ED, Shilo B-Z. 2016. The Drosophila formin Fhos is a primary
1044 mediator of sarcomeric thin-filament array assembly. *eLife Sciences* **5**:e16540.
1045 doi:10.7554/eLife.16540
1046 Smith MB, Li H, Shen T, Huang X, Yusuf E, Vavylonis D. 2010. Segmentation and tracking of
1047 cytoskeletal filaments using open active contours. *Cytoskeleton (Hoboken)* **67**:693–705.
1048 doi:10.1002/cm.20481
1049 Spudich JA, Watt S. 1971. The Regulation of Rabbit Skeletal Muscle Contraction. *Journal of*
1050 *Biological Chemistry* **246**:4866–4871. doi:10.1016/S0021-9258(18)62016-2
1051 Stringer C, Wang T, Michaelos M, Pachitariu M. 2021. Cellpose: a generalist algorithm for
1052 cellular segmentation. *Nat Methods* **18**:100–106. doi:10.1038/s41592-020-01018-x
1053 Sun H, Luo Y, Miao Y. 2018. Purification of Globular Actin from Rabbit Muscle and Pyrene
1054 Fluorescent Assays to Investigate Actin Dynamics in vitro. *Bio Protoc* **8**:e3102.
1055 doi:10.21769/BioProtoc.3102

1056 Sundaramurthy S, Votra S, Laszlo A, Davies T, Pruyne D. 2020. FHOD-1 is the only formin in
1057 Caenorhabditis elegans that promotes striated muscle growth and Z-line organization in
1058 a cell autonomous manner. *Cytoskeleton* **77**:422–441. doi:10.1002/cm.21639
1059 Svitkina T. 2018. The Actin Cytoskeleton and Actin-Based Motility. *Cold Spring Harb Perspect*
1060 *Biol* **10**:a018267. doi:10.1101/cshperspect.a018267
1061 Szikora S, Görög P, Mihály J. 2022. The Mechanisms of Thin Filament Assembly and Length
1062 Regulation in Muscles. *International Journal of Molecular Sciences* **23**:5306.
1063 doi:10.3390/ijms23105306
1064 Taniguchi K, Takeya R, Suetsugu S, Kan-o M, Narusawa M, Shiose A, Tominaga R, Sumimoto H.
1065 2009. Mammalian formin Fhod3 regulates actin assembly and sarcomere organization in
1066 striated muscles. *Journal of Biological Chemistry* **284**:29873–29881.
1067 doi:10.1074/jbc.M109.059303
1068 Ushijima T, Fujimoto N, Matsuyama S, Kan-o M, Kiyonari H, Shioi G, Kage Y, Yamasaki S, Takeya
1069 R, Sumimoto H. 2018. The actin-organizing formin protein Fhod3 is required for
1070 postnatal development and functional maintenance of the adult heart in mice. *J Biol*
1071 *Chem* **293**:148–162. doi:10.1074/jbc.M117.813931
1072 Vizcarra CL, Bor B, Quinlan ME. 2014. The Role of Formin Tails in Actin Nucleation, Processive
1073 Elongation, and Filament Bundling. *J Biol Chem* **289**:30602–30613.
1074 doi:10.1074/jbc.M114.588368
1075 Vodnjov N, Toplišek J, Maver A, Čuturilo G, Jaklič H, Teran N, Višnjar T, Pušenjak MŠ, Hodžić A,
1076 Miljanović O, Peterlin B, Writzl K. 2023. A novel splice-site FHOD3 founder variant is a
1077 common cause of hypertrophic cardiomyopathy in the population of the Balkans–A
1078 cohort study. *PLOS ONE* **18**:e0294969. doi:10.1371/journal.pone.0294969
1079 Wu G, Ruan J, Liu J, Zhang C, Kang L, Wang J, Zou Y, Song L. 2021. Variant Spectrum of Formin
1080 Homology 2 Domain-Containing 3 Gene in Chinese Patients With Hypertrophic
1081 Cardiomyopathy. *Journal of the American Heart Association* **10**:e018236.
1082 doi:10.1161/JAHA.120.018236
1083 Xu Y, Moseley JB, Sagot I, Poy F, Pellman D, Goode BL, Eck MJ. 2004. Crystal Structures of a
1084 Formin Homology-2 Domain Reveal a Tethered Dimer Architecture. *Cell* **116**:711–723.
1085 doi:10.1016/S0092-8674(04)00210-7
1086 Zweifel ME, Courtemanche N. 2020. Competition for delivery of profilin–actin to barbed ends
1087 limits the rate of formin-mediated actin filament elongation. *J Biol Chem* **295**:4513–
1088 4525. doi:10.1074/jbc.RA119.012000
1089
1090

Figure 1

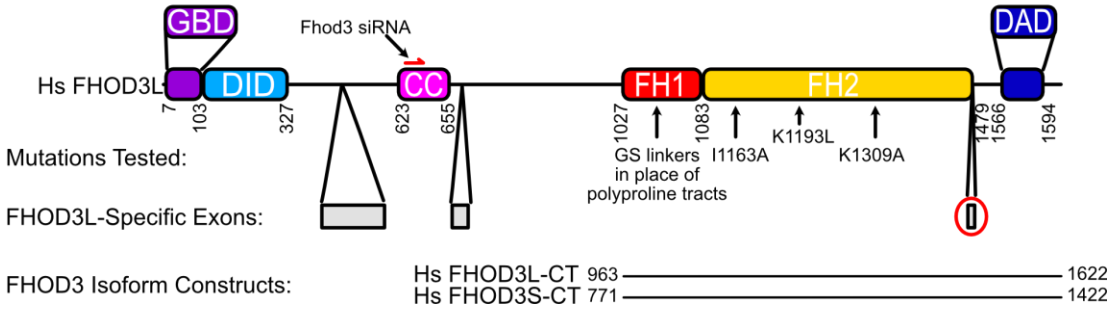

Figure 1. Domain structure of human FHOD3. GDB=GTP Binding Domain, DID=Diaphanous Inhibitory Domain, CC=Coiled-coil, FH=Formin Homology, DAD=Diaphanous Autoregulatory Domain. Mutations tested in this study are indicated with black arrows. Numbers correspond to FHOD 3L sequence (Uniprot Isoform 4). The FHOD3L construct spans residues 963–1622 and includes the FH1 domain, FH2 domain, and tail. The FHOD3S construct spans residues 771-1422 (Uniprot Isoform 1 numbering). FHOD3L-specific exons are in gray. The 8-residue $T(D/E)_5XE$ exon that distinguishes FHOD3L-CT from FHOD3S-CT is circled in red.

Figure 1 Supplement 1

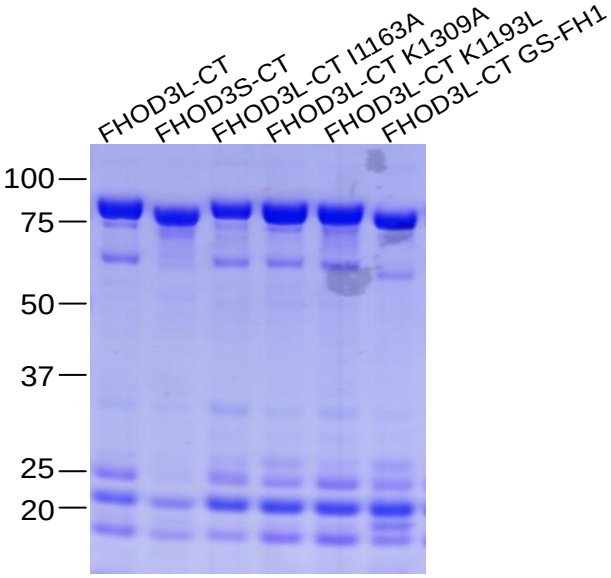

Figure 1—figure supplement 1. Coomassie-stained polyacrylamide gel showing purified FHOD3 constructs. Lower molecular weight contaminants were difficult to remove without significantly diluting the sample. They were relatively consistent for each construct, and had no detectable impact on FHOD activity.

Figure 2

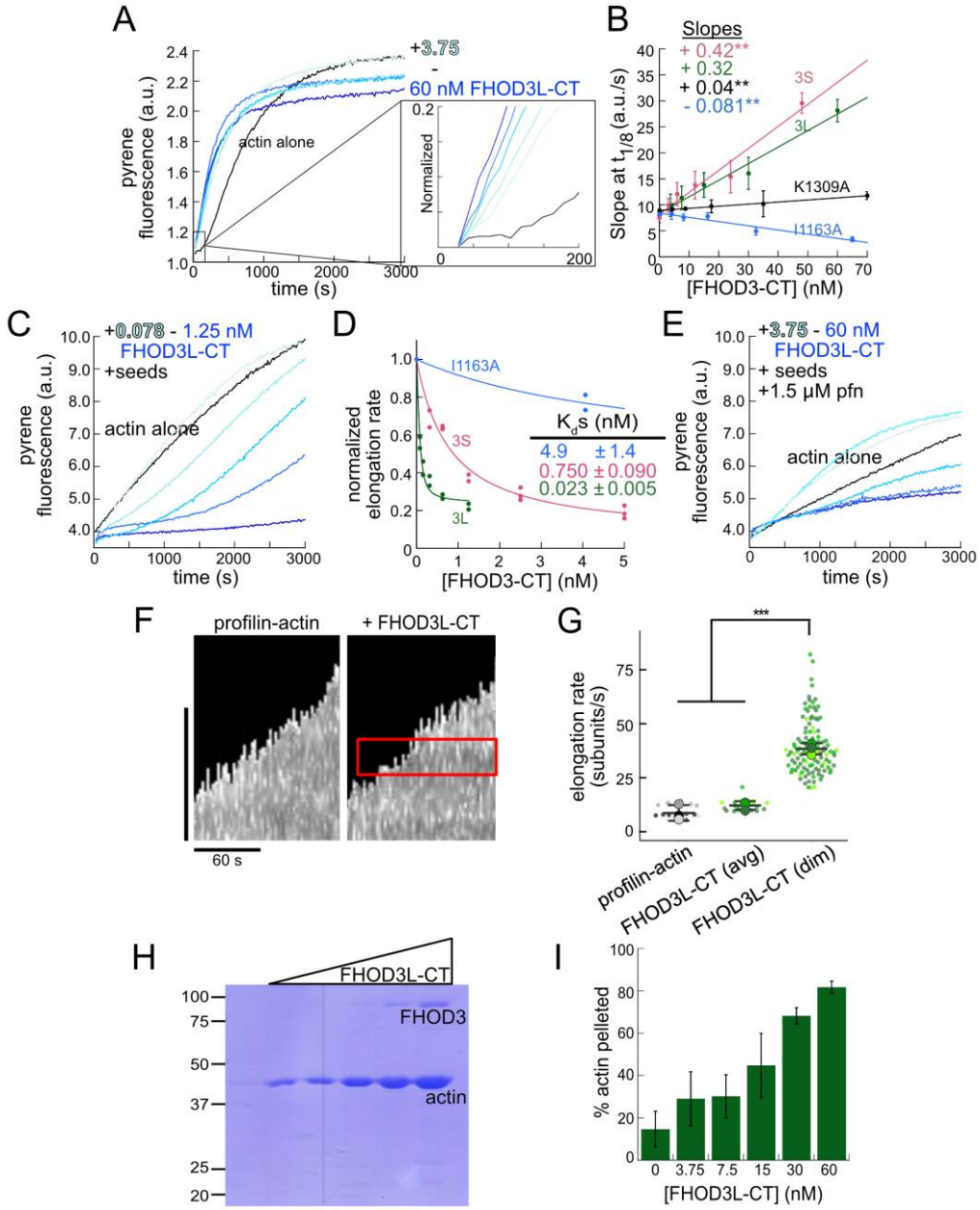

Figure 2. Biochemical characterization of human FHOD3L. (**A**) Assembly of 4 µM actin (5% pyrene-labeled) and the indicated concentrations of FHOD3L-CT from a 2-fold dilution series. The inset shows the first 200 seconds of data normalized to the plateau of actin alone. (**B**) Relative nucleation activities of FHOD3L-CT (n=5), FHOD3S-CT (n=4), FHOD3L-CT K1309A (n=3) and I1163A (n=3). Data are means ± SD. Slopes reported are the average slopes of independent experiments. The asterisks indicate significance of difference from FHOD3L-CT (see below for details). (**C**) Barbed-end elongation assay. Final conditions were 0.25 µM F-actin seeds (~0.1 nM barbed ends), 0.5 µM actin (10% pyrene-labeled), and indicated concentrations FHOD3L-CT. (**D**) Quantification of barbed-end affinity for FHOD3L-CT (from **C**), FHOD3S-CT (from Figure 2, figure supplement 2B) and FHOD3L-CT I1163A. Raw data are shown

and the lines are fits to all data points. The K_ds reported are the averages of three independent trials. (n=3, each; mean ± SD.) (**E**) Barbed-end elongation assay with profilin. Final conditions as in (**C**) plus 1.5 µM *S. pombe* profilin. (**F**) Kymographs of growing filaments from TIRF assays with or without FHOD3L-CT. Conditions: 1 µM actin (10%-Alexa Fluor 488-labeled), 5 µM Hs profilin-1 ± 0.1 nM FHOD3L-CT. The red box highlights a pause followed by a burst of elongation. Vertical scale bar, 5 µm. (**G**) Elongation rates from TIRF assays. Average elongation rates (over 10s of seconds) and formin-mediated elongation rates (dim) are shown separately. (n=21, profilin-actin; n=20, FHOD3L-CT (avg); n=112, FHOD3L-CT (dim); 3 channels for all samples; mean ± SD.) Scale bars, 10 µm. (**H**) Coomassie-stained polyacrylamide gel of pellet fractions from low-speed bundling assays with 5 µM actin and 0-60 nM FHOD3L-CT. (**I**) Quantification of bundling from (**H**) via densitometry (n=3 each; mean ± SD.) p-values were determined by one-way ANOVA with post-hoc Tukey test. ** $p < 0.001$, *** $p < 0.0001$.

Figure 2 - supplement 1

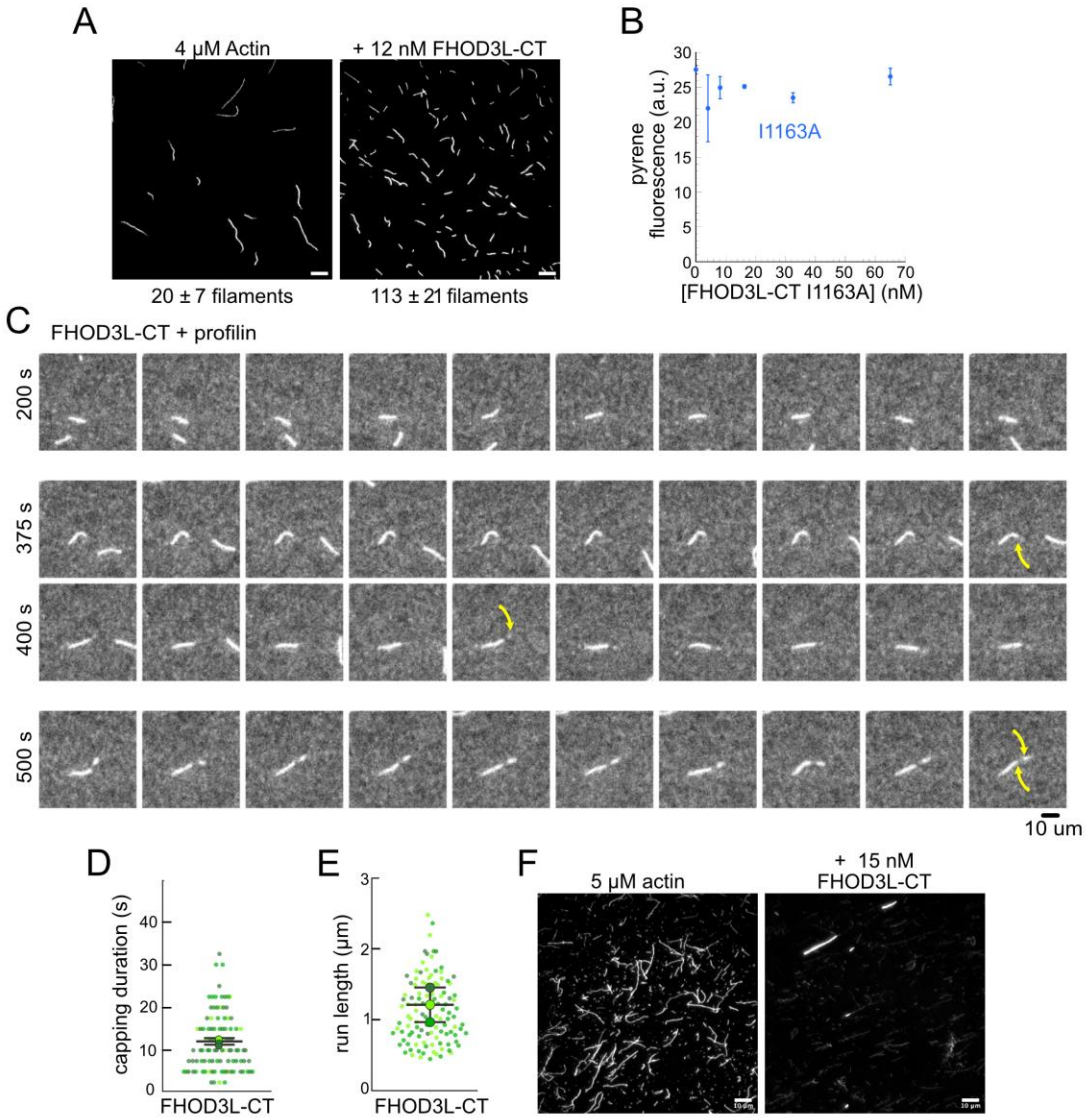

Figure 2—figure supplement 1 (A) Actin polymerized in the presence or absence of 12 nM FHOD3L-CT, stabilized with fluorescent phalloidin and diluted to 5 nM. (n=3, each; mean ± SD) Scale bars, 10 µm. (**B**) Pyrene fluorescence readings of 4 µM actin filaments (5% pyrene-labeled) incubated with different concentrations of FHOD3L-CT I1163A for 5 minutes. (n=2; mean ± SD.) **(C)** Time-lapse images from TIRF microscopy. Conditions: 1 µM actin (10%-Alexa Fluor 488-labeled), 5 µM Hs profilin-1 ± 0.1 nM FHOD3L-CT. Yellow arrows indicate beginning and end of dim portion of filament elongated by FHOD3L-CT. 2.5 s / frame. Scale bar, 10 µm. (**D**) Duration of pauses observed in TIRF assays. (**F**) Run lengths observed in TIRF assays. (For (**D-E**) n=112 (dim); 3 flow channels; mean ± SD.) **(E)** Epifluorescence micrographs of phalloidin-stabilized filaments from low-speed bundling assays. Conditions: 5 µM actin filaments with or without 15 nM FHOD3L-CT, diluted to 5 nM actin after centrifugation. Scale bars, 10 µm.

Figure 2 Supplement 2

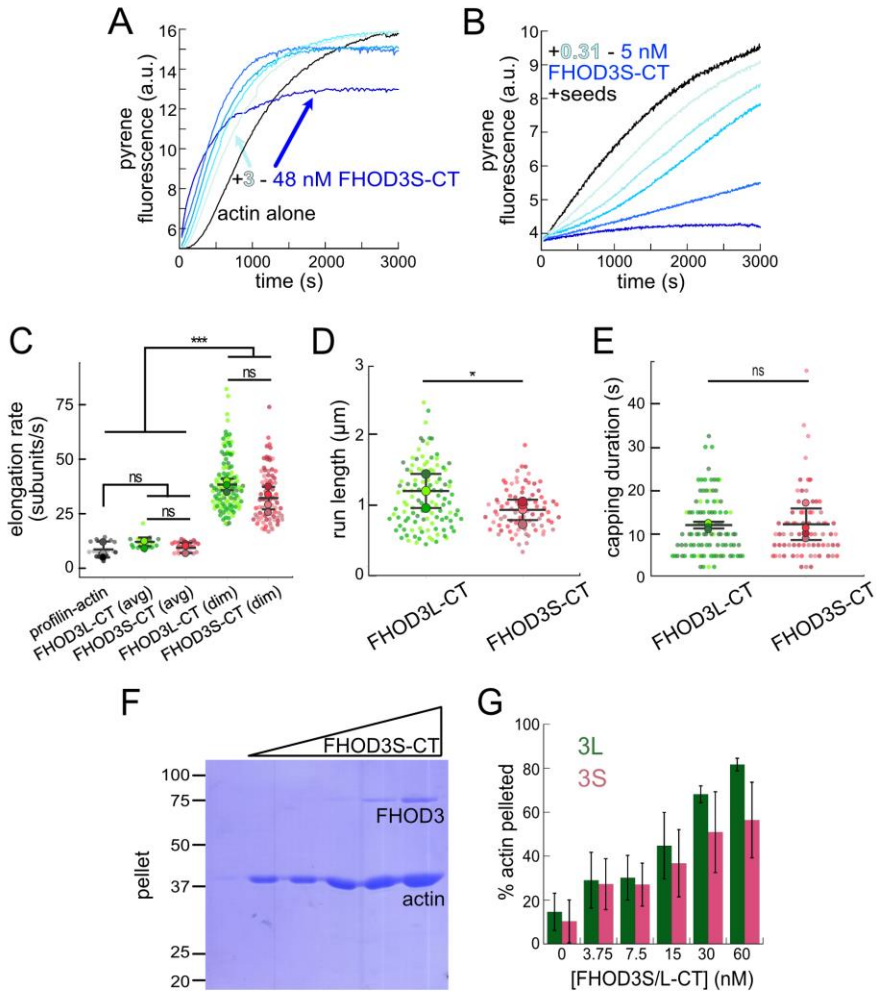

Figure 2—figure supplement 2. Comparison of FHOD3S to FHOD3L. (**A**) Assembly of 4 µM actin (5% pyrene-labeled) and the indicated concentrations of FHOD3S from a 2-fold dilution series. (**B**) Barbed-end elongation assay. Final conditions: 0.25 µM F-actin seeds (~0.1 nM barbed ends), 0.5 µM G-actin (10% pyrene-labeled), and 312.5 pM-5 nM FHOD3S-CT. (**C**) Elongation rates from TIRF assays. Average elongation rates (over 10s of seconds) and formin-mediated elongation rates (dim) are shown separately. Conditions: 1 µM actin (10%-Alexa Fluor 488-labeled), 5 µM Hs profilin-1 ± 0.1 nM FHOD3L-CT or 1 nM FHOD3S-CT. (profilin-actin n=21; 3L (avg) n=20; 3S (avg) n=24; 3L (dim) n=112; 3S (dim) n=78; 4 flow channels for 3S, 3 flow channels for all others; mean ± SD, p-values by one-way ANOVA with post-hoc Tukey test.) (**D**) Quantification of (dim) run lengths for FHOD3S/L-CT TIRF assays. (FHOD3L-CT n=97; FHOD3S-CT n=73; 3 flow channels for 3L, 4 flow channels for 3S; mean ± SD, p-values by Mann-Whitney U test.) (**E**) Duration of capping events by FHOD3L-CT vs FHOD3S-CT observed by TIRF microscopy. (FHOD3L-CT n=97; FHOD3S-CT n=73; 3 flow channels for 3L, 4 flow channels for 3S; mean ± SD, p-values by Mann-Whitney U test.) (**F**) Coomassie-stained polyacrylamide gel of pellet fractions from low-speed bundling assays with 5 µM actin and 0-60 nM FHOD3S-CT. (**H**) Comparison of bundling for FHOD3S/L-CT via densitometry (n=3 each group; mean ± SD.) ns $p > 0.05$, * $p < 0.05$, *** $p < 0.0001$

Figure 3

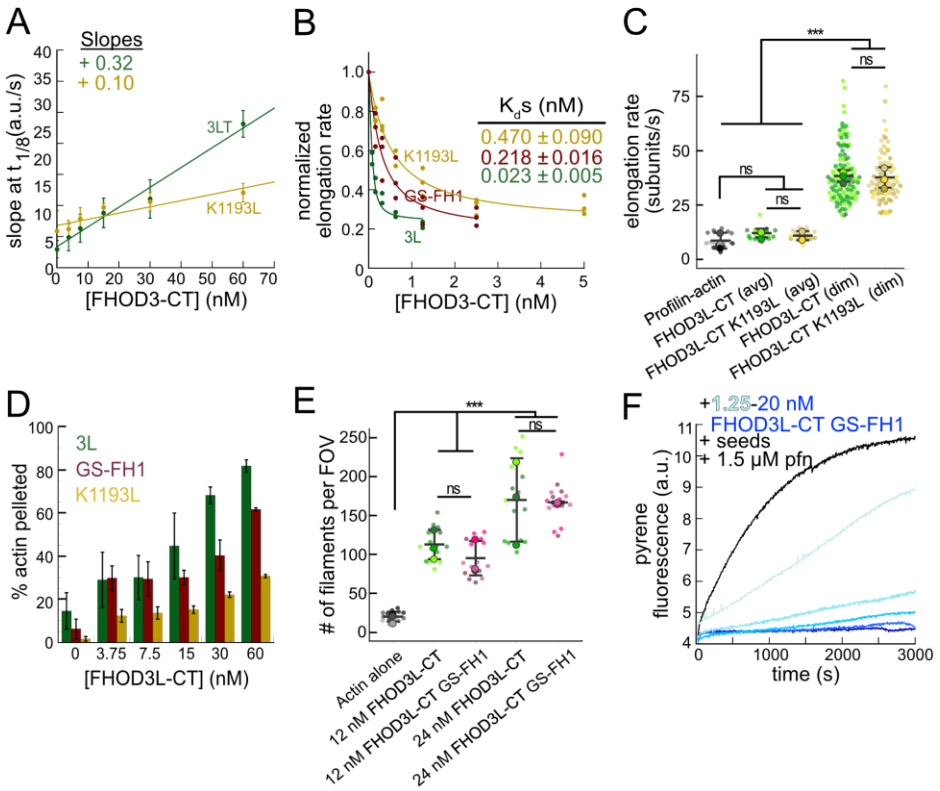

Figure 3. Biochemical validation of function-separating mutants. (**A**) Relative nucleation activity for FHOD3L-CT (n=5) and FHOD3L-CT K1193L (n=5). Data points are means and error bars are standard deviations. Slopes reported are the average slopes of independent experiments. (**B**) Barbed-end affinity measurements for FHOD3L-CT, FHOD3L-CT GS-FH1, and FHOD3L-CT K1193L. Raw data are shown and the line is a fit to all data points. The K_ds reported are the average of three independent trials. (n=3, each; mean ± SD.) (**C**) Elongation rates from TIRF assays. Conditions: 1 μM actin (10%-Alexa Fluor 488-labeled), 5 μM Hs profilin-1 ± 0.1 nM FHOD3L-CT or 1 nM FHOD3L-CT K1193L. Average elongation rates (over 10s of seconds) and formin-mediated elongation rates (dim) are shown separately. (FHOD3L-CT K1193L (avg) n=19; FHOD3L-CT K1193L (dim) n=67; 3 flow channels each; mean ± SD, p-values by one-way ANOVA with post-hoc Tukey test.) (**D**) Quantification of bundling by FHOD3L-CT GS-FH1 and K1193L (n=3, each; mean ± SD.) (**E**) Nucleation test. Quantification of number of filaments per FOV for FHOD3L-CT and FHOD3L-CT GS-FH1. Conditions: 4 μM actin with indicated construct. Reaction was stabilized with Alexa488-phalloidin and diluted to 5 nM actin for visualization. 5 images (technical replicates) were taken per independent experiment. (n=15 images each; 3 biological replicates each; mean ± SD, p-values by one-way ANOVA with post-hoc Tukey test.) Representative images are shown in Figure 3-supplement 1D. (**F**) Barbed-end elongation assay for FHOD3L-CT GS-FH1 in the presence of profilin. Final conditions: 0.25 μM F-actin seeds (~0.1 nM barbed ends), 0.5 μM actin (10% pyrene-labeled), 1.5 μM *S. pombe* profilin, and 1.25 nM-20 nM FHOD3L-CT GS-FH1. (n=2; mean ± SD.) ns $p > 0.05$, *** $p < 0.0001$

Figure 3 Supplement 1

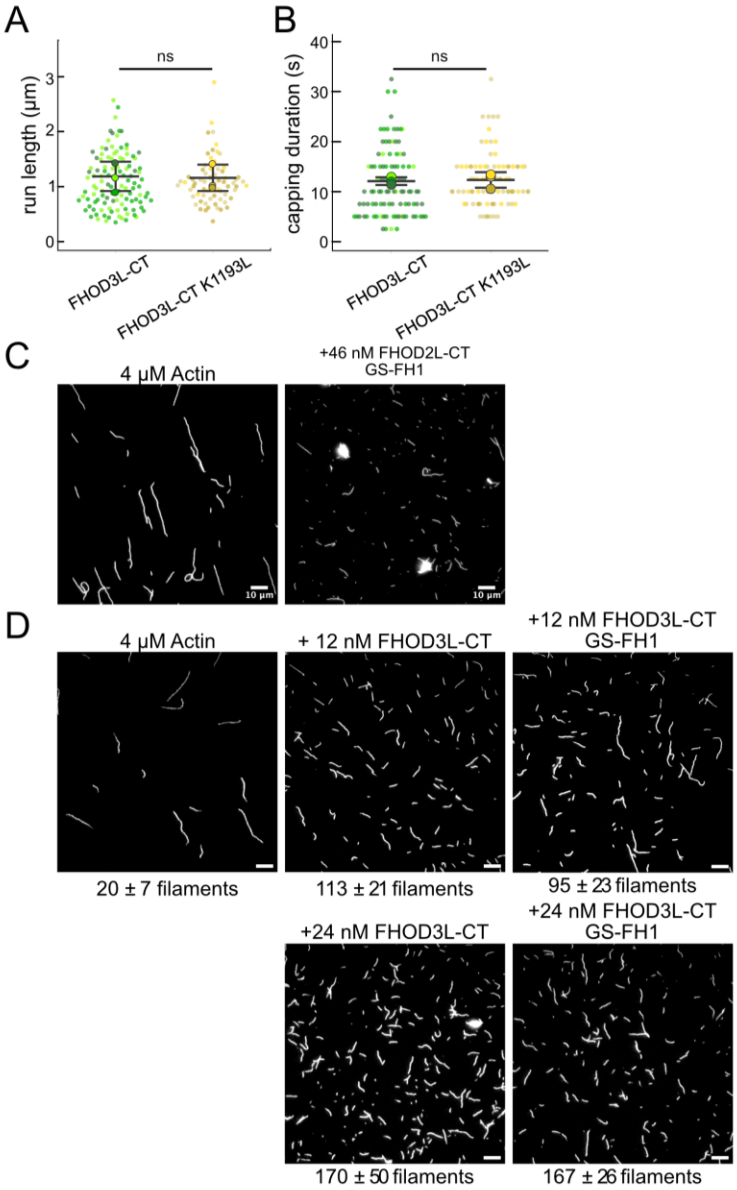

Figure 3—figure supplement 1. (**A**) Quantification of run lengths for FHOD3L-CT and FHOD3L-CT K1193L. ($p>0.05$ by Mann-Whitney U test.) (**B**) Duration of capping events by FHOD3L-CT and FHOD3L-CT K1193L observed by TIRF microscopy. ($p>0.05$ by Mann-Whitney U test.) (**C**) TIRF micrographs from nucleation assays using 4 µM actin in the presence or absence of 46 nM FHOD3L-CT GS-FH1, stabilized with Alexa488-phalloiding and diluted to 5 nM. (**D**) TIRF micrographs from nucleation assays using 4 µM actin and indicated concentration of FHOD3 construct. Samples were diluted to 5 nM actin in Alexa488 phalloidin for visualization. The number of aggregates was negligible at lower concentrations of FHOD3L-CT GS-FH1. Quantification shown in Figure 3E.

Figure 4

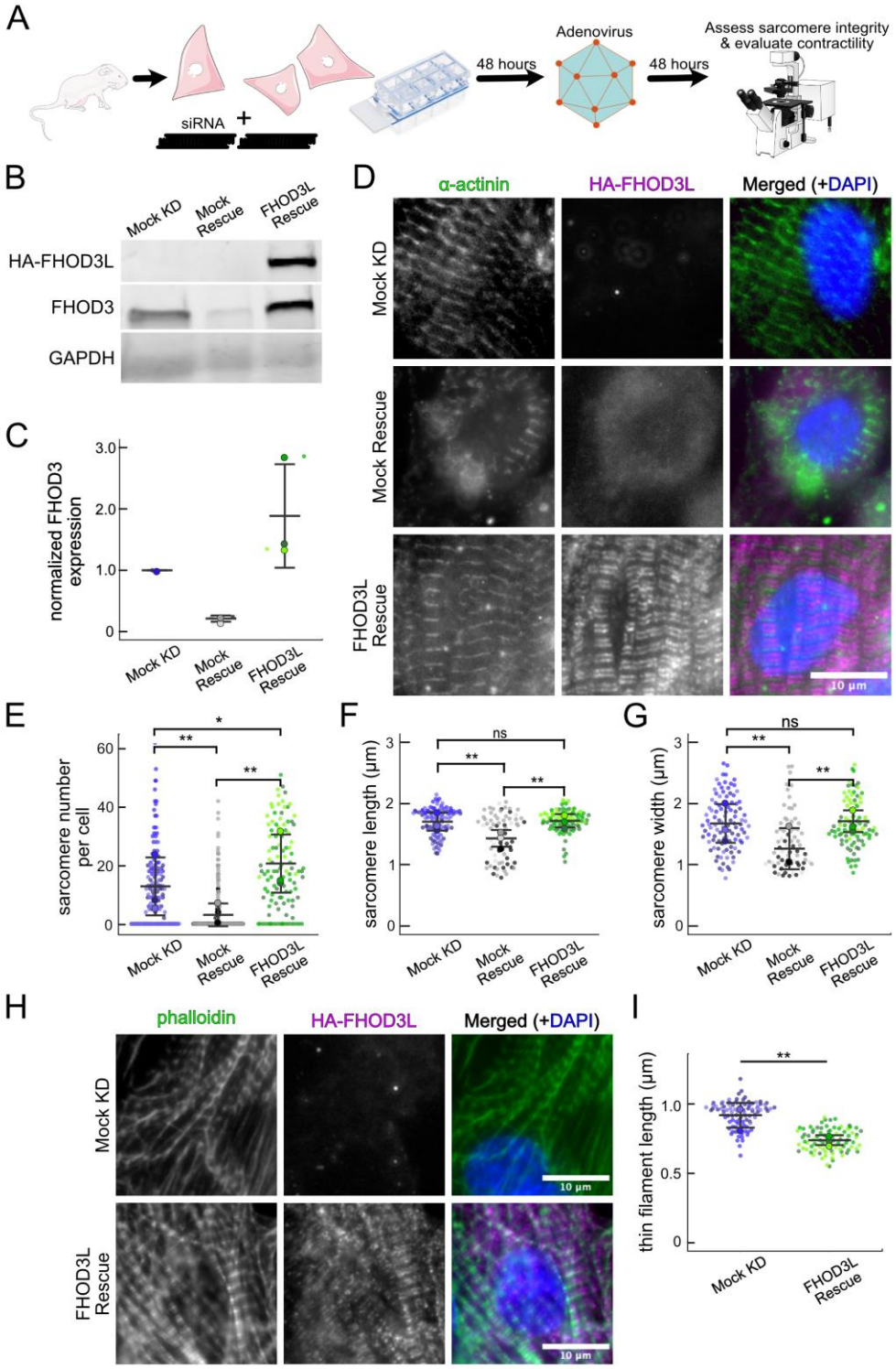

Figure 4. FHOD3L rescues sarcomere organization in neonatal rat ventricular myocytes. (**A**) Overview of the rescue experiments. Reverse transfection of siRNA upon plating NRVMs followed by infection with adenovirus to drive exogenous expression. (**B**) Western blot showing depletion of

endogenous FHOD3 after knockdown, and exogenous FHOD3L expression levels after rescue. GAPDH used as a loading control. (**C**) Quantification of Western blot in (**B**) normalized to GAPDH for each lane and then normalized to endogenous levels in the mock knockdown. (n=3, each; mean $\pm$ SD.) (**D**) Sarcomere integrity indicated by immunofluorescent staining of α-actinin (green). Localization of exogenous HA-FHOD3L is shown in magenta. DAPI (blue) is included in the merged images. WGA is not shown for clarity. (**E**) Quantification of sarcomere number per NRVM. (n=160 cells, mock KD; n=334 cells, mock rescue; n=110 cells, FHOD3L rescue.) (**F**) Average sarcomere lengths per NRVM. (mock KD n=100 cells; mock rescue n=71 cells; FHOD3L rescue n=92 cells). (**G**) Average sarcomere widths (Z-line lengths) per NRVM. (mock KD n=100 cells; mock rescue n=71 cells; FHOD3L rescue n=92 cells) (**H**) Epifluorescence micrographs showing mock knockdown and FHOD3L-rescued NRVMs stained with phalloidin (green) to visualize thin filaments and anti-HA (magenta) to show expression of exogenous FHOD3L. (**I**) Quantification of thin filament lengths for mock knockdown and FHOD3L-rescued NRVMs. (mock KD n=94 cells; WT rescue n=84 cells) For (**E,F,G,I**) Data from three biological replicates for each condition are represented by different shades. Mean $\pm$ SD is shown. p-values were calculated with Mann-Whitney U tests, ns $p > 0.05$; * $p < 0.05$; ** $p < 0.001$.

Figure 4 - Supplement 1

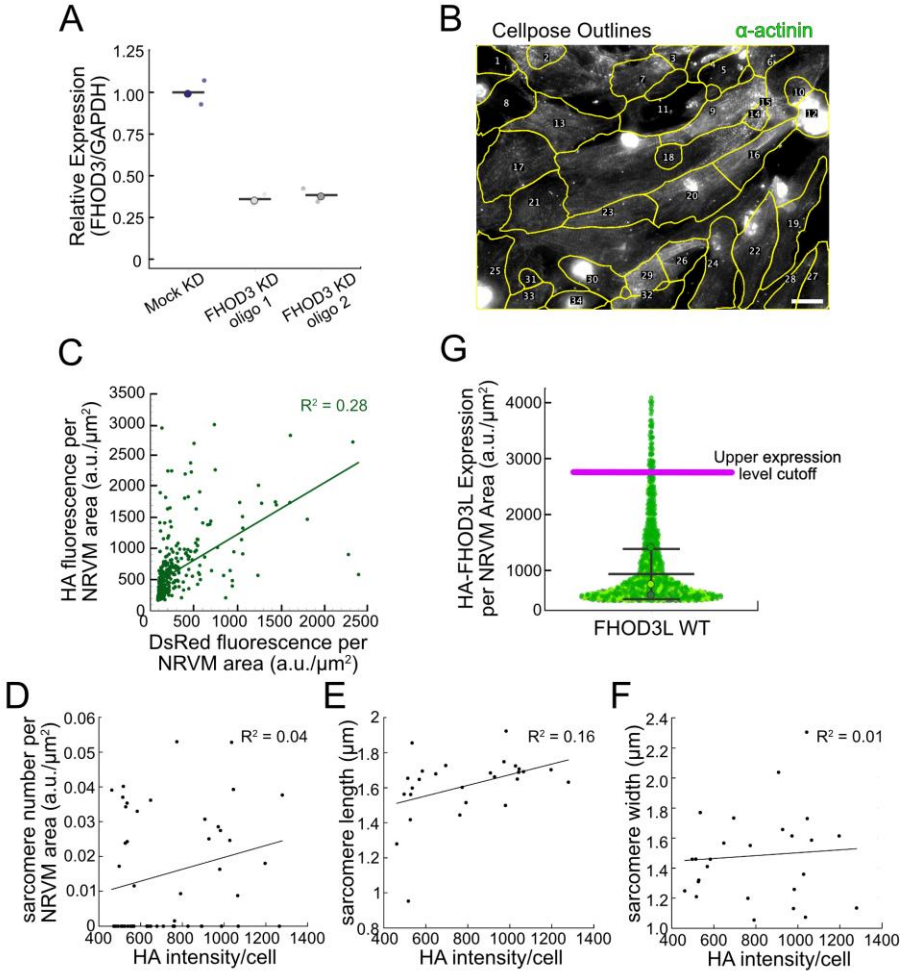

Figure 4—figure supplement 1. Method establishment for FHOD3L rescues in neonatal rat ventricular myocytes. **(A)** Relative mRNA expression of *FHOD3* in NRVMs after knockdown with different siRNA oligos compared to *GAPDH* mRNA expression (n=2 wells, 1 biological replicate; mean)**.** (**B**) Typical image of cellpose segmentation of wild-type FHOD3L-rescued NRVMs, used for per cell quantification of sarcomeres. ROI's are numbered. Scale bar, 20 µm (**C**) Pairwise correlation of normalized DsRed vs. HA fluorescence intensity from FHOD3L rescue, plotted per NRVM area. Correlation is too weak to use DsRed as an expression level reporter (n=347 cells; 1 biological replicate). (D-F) Pairwise correlation of HA fluorescence intensity vs. (D) sarcomere number, (E) sarcomere length, (F) sarcomere width from FHOD3L rescue, plotted per NRVM area. (**G**) Normalized and background corrected 3xHA-FHOD3L fluorescence intensity per NRVM area from a rescue experiment. Magenta line indicates the upper expression level cutoff (2700 a.u./µm^2) used to select cells for further analysis (n=913 cells; 3 biological replicates; mean $\pm$ SD.)

Figure 5

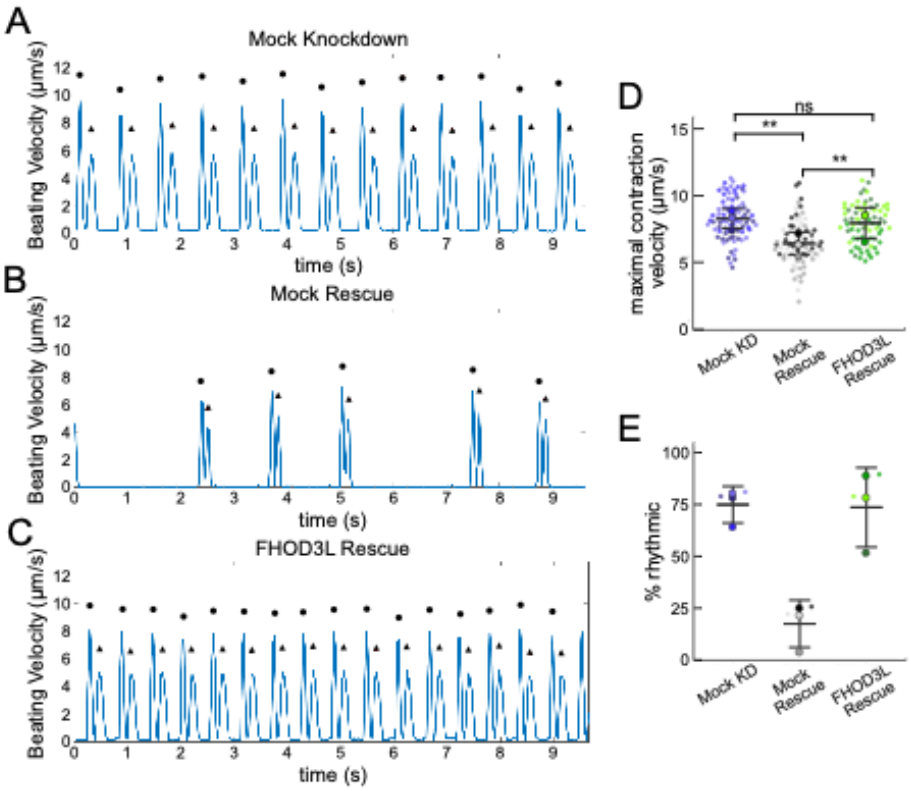

Figure 5. FHOD3L rescues contractility in neonatal rat ventricular myocytes. (**A-C**) Motion analysis by digital image correlation. Mock knockdown, mock rescue, and FHOD3L rescue beating patterns are shown. The first (•) and the second (▲) peak of each duplex represent the contraction and the relaxation speed, respectively. (**D**) Maximal contraction velocities quantified for mock knockdown, mock rescue, and FHOD3L wild-type rescue (mock KD n=82 ROIs; mock rescue n=81 ROIs; FHOD3L rescue n=72 ROIs; 3 biological replicates, each; mean ± SD, p-values by Student's two-sample, unpaired t-test.) (**E**) Quantification of the percentage of analyzed ROI's from the videos that contained rhythmic contractions for mock knockdown, mock rescue, and FHOD3L wild-type rescue. (n=3, each; mean ± SD.) (Note, we did not analyze % rhythmicity because the data rely on percentages. Thus only large changes are noted.) ns $p > 0.05$, ** $p < 0.001$.

Figure 5 Supplement 1

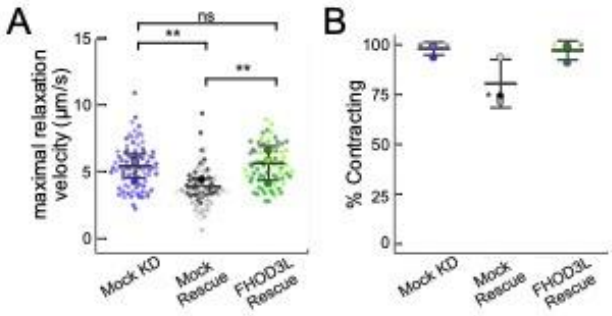

Figure 5—figure supplement 1. (**A**) Maximal relaxation velocities quantified for mock knockdown, mock rescue, and FHOD3L rescue (mock KD n=82 ROIs; mock rescue n=81 ROIs; FHOD3L rescue n=72 ROIs; 3 biological replicates, each; mean ± SD, p-values by Student's two-sample, unpaired t-test.) (**B**) Estimate of the percentage of NRVMs contracting in each video for mock knockdown, mock rescue, and FHOD3L rescue. (n=3, each; mean ± SD.) (Note, we did not statistically analyze the % contracting data because they are a subjective measurement. Thus, only large changes are noted.) p-values determined with Student's two-sample, unpaired t-test. * $p < 0.05$, ** $p < 0.001$, *** $p < 0.0001$

Figure 5 Supplement 2

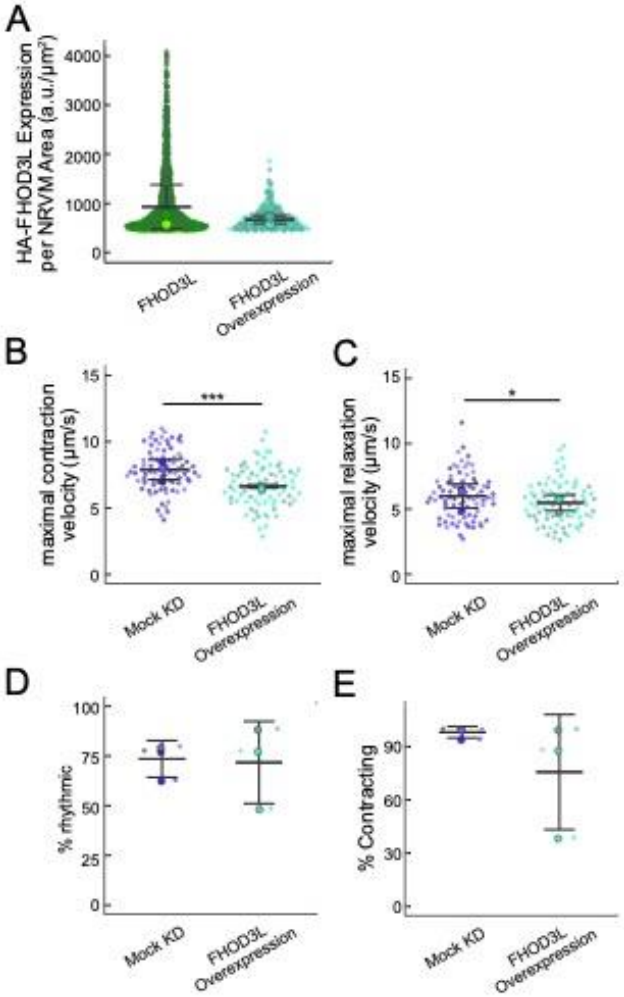

Figure 5—figure supplement 2. (**A**) Comparison of 3xHA-FHOD3L fluorescence intensity per NRVM area from a rescue experiment and an overexpression experiment. Data are normalized and background corrected as in Fig.4-supplemental figure 1G. (**B**) Maximal contraction velocities quantified for mock knockdown and FHOD3L overexpression NRVMs (mock KD n=82 ROIs; FHOD3L overexpression n=79 ROIs; 3 biological replicates, each; mean ± SD, p-value by Student's two-sample, unpaired t-test.) (**C**) Maximal relaxation velocities quantified for mock knockdown and FHOD3L overexpression NRVMs (mock KD n=82 ROIs; FHOD3L overexpression n=79 ROIs; 3 biological replicates, each; mean ± SD, p-value by student's two-sample, unpaired t-test.) (**D**) Quantification of rhythmic contractions as in Fig. 5E for mock knockdown and overexpression NRVMs (n=3, each; mean ± SD.) (**E**) Estimate of the percentage of NRVMs contracting in each video for mock knockdown and overexpression NRVMs (n=3, each; mean ± SD.) * $p < 0.05$, ** $p < 0.001$, *** $p < 0.0001$

Figure 6

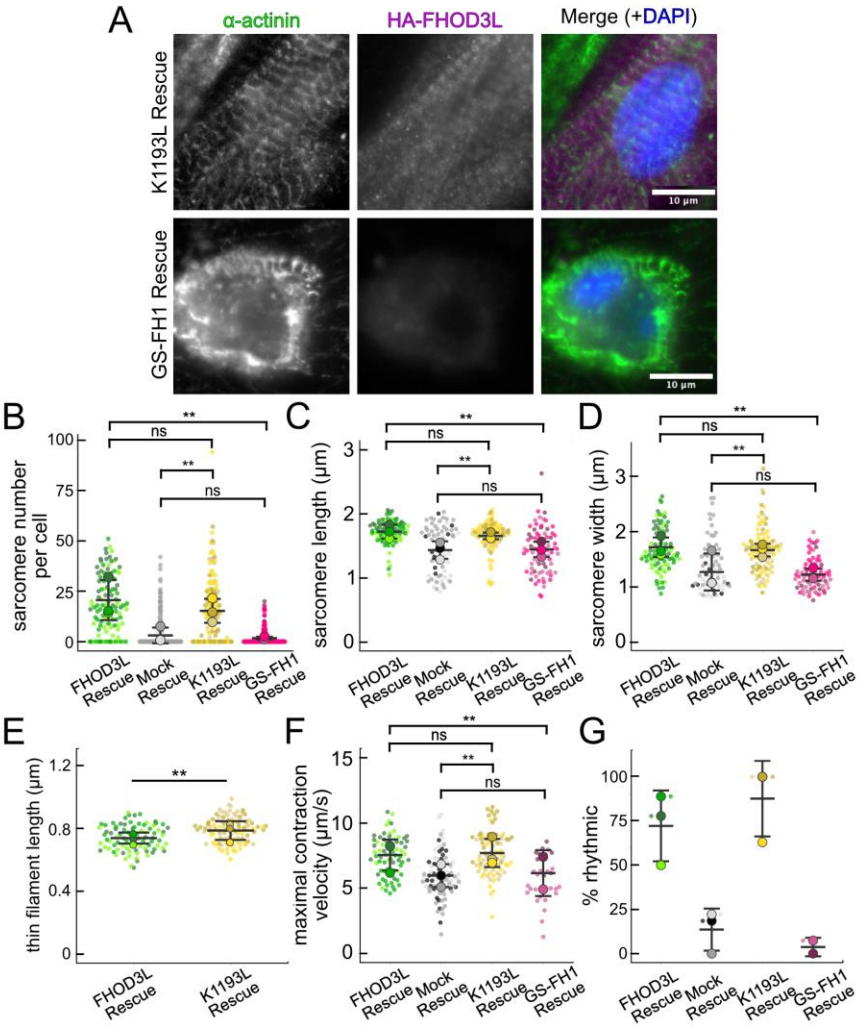

Figure 6. Loss of nucleation but not elongation is tolerated for sarcomere formation and function. (**A**) Images of NRVMs rescued with K1193L or GS-FH1. Sarcomere integrity indicated by immunofluorescent staining of α-actinin (green). Localization of exogenous FHOD3L is shown in magenta. DAPI (blue) is included in the merged images. WGA is not shown for clarity. (**B**) Quantification of sarcomere number per NRVM in the FHOD3L, K1193L, and GS-FH1 rescues. (K1193L n=148 cells; GS-FH1 n=259 cells; 3 biological replicates; mean ± SD, p-values by Mann-Whitney-U test.) (**C**) Average sarcomere lengths per NRVM in the FHOD3L, K1193L, and GS-FH1-rescues. (K1193L n=95 cells; GS-FH1 n=73 cells; 3 biological replicates; mean ± SD, p-value for FHOD3L comparison to GS-FH1 by Student's two-sample, unpaired t-test, all other p-values by Mann-Whitney-U test.) (**D**) Average sarcomere widths (Z-line lengths) per NRVM in the FHOD3L, K1193L, and GS-FH1-rescues. (K1193L n=95 cells; GS-FH1 n=73 cells; 3 biological replicates; mean ± SD, p-values by Mann-Whitney-U test.) (**E**) Quantification of thin filament lengths for FHOD3L and K1193L-rescued NRVMs (K1193L n=99 cells; 3 biological replicates, each; mean ± SD, p-value by Mann-Whitney-U test.) (**G**) Quantification of contracting NRVMs as in Fig. 5D for FHOD3L, K1193L, and GS-FH1-rescued NRVMs. (n=3, each; mean ± SD.) (**H**) Quantification of rhythmic contractions as in Fig. 5E for FHOD3L, K1193L, and GS-FH1-rescued NRVMs. (FHOD3L n=3; K1193L n=3; GS-FH1 n=2; mean ± SD.) ns $p > 0.05$, ** $p < 0.001$

Figure 6 - Supplement 1

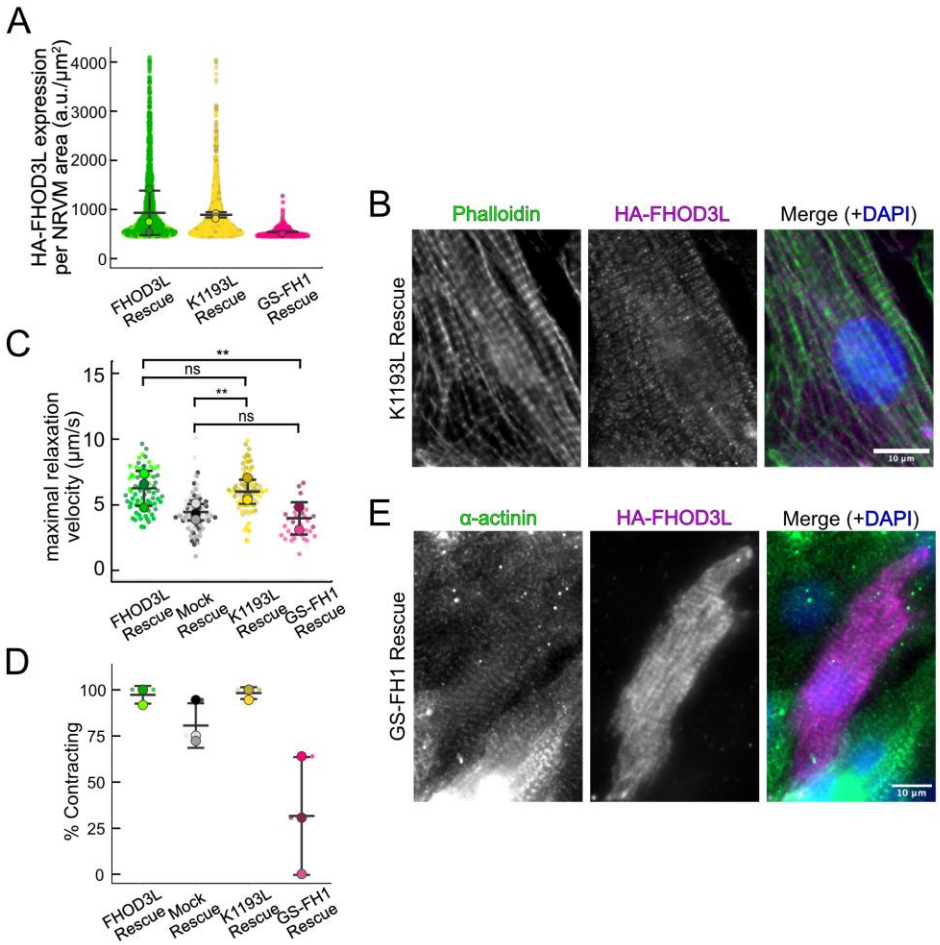

Figure 6—figure supplement 1. (A) Normalized and background-corrected fluorescence intensity per NRVM area from the FHOD3L, K1193L, and GS-FH1 rescues. (K1193L n=897 cells; GS-FH1 n=536 cells; 3 biological replicates, each; mean ± SD.) (**B**) Epifluorescence micrographs showing K1193L-rescued NRVMs stained with phalloidin (green) to visualize thin filaments and anti-HA (magenta) to show expression of exogenous FHOD3L. (**C**) Maximal relaxation velocities for FHOD3L, K1193L, and GS-FH1-rescued NRVMs. (K1193L n=81 ROIs; GS-FH1 n=31 ROIs; 3 biological replicates for WT and K1193L; 2 for GS-FH1; mean ± SD, p-values from Mann-Whitney U test.) (**D**) Maximal contraction velocities quantified for FHOD3L, K1193L, and GS-FH1-rescued NRVMs. (K1193L n=81 ROIs; GS-FH1 n=31 ROIs; 3 biological replicates, WT and K1193L; 2 for GS-FH1; mean ± SD; p-values determined with Mann-Whitney-U test.) (**E**) Striated HA-FHOD3L demonstrates that the GS-FH1 mutant can localize correctly if sarcomeres are present. Sarcomere integrity indicated by immunofluorescent staining of α-actinin (green). Localization of exogenous HA-FHOD3L is shown in magenta. DAPI (blue) is included in the merged images. WGA is not shown for clarity. ns $p > 0.05$, ** $p < 0.001$

	Pyrene-actin-based assays		TIRF-based assays			Cosedimentation
	Nucleation Strength (a.u./s)	Barbed end binding affinity (nM)	Elongation Rate (subunits/s)	Run Length (µm)	Capping duration (s)	Bundling (% actin pelleted at 60 nM)
FHOD3L-CT	0.32 ± 0.04 (n=5)	0.028 ± 0.005	39 ± 13	1.10 ± 0.49	11.8 ± 6.8	81.7 ± 2.9
FHOD3S-CT	0.42 ± 0.04* (n=4)	0.750 ± 0.090*	33 ± 12	0.90 ± 0.33*	12.0 ± 7.8	56 ± 17
FHOD3L-CT I1163A	-0.081 ± 0.002* (n=3)	4.9 ± 1.4*	n.d.	n.d.	n.d.	n.d.
FHOD3L-CT K1309A	0.04 ± 0.02* (n=3)	n.d.	n.d.	n.d.	n.d.	n.d.
FHOD3L-CT K1193L	0.10 ± 0.02* (n=5)	0.470 ± 0.090*	38 ± 12	1.11 ± 0.42	12.7 ± 5.6	30.8 ± 0.7
FHOD3L-CT GS-FH1	Nucleates similarly via TIRF nucleation assay	0.218 ± 0.016*	n.d.	n.d.	n.d.	61.7 ± 0.7

Table 1: Summary of biochemical measurements for FHOD3L-CT and mutants. All data shown are means ± standard deviation each from 3 independent experiments, unless otherwise indicated. n.d.= no data. Light grey columns are data acquired with bulk pyrene-actin based assays without profilin added. Medium grey columns provide data from TIRF analysis of individual filaments (profilin was present). The dark grey column reports data from cosedimentation assay.
* Statistically different from FHOD3L-CT. Analysis by ANOVA and Tukey post hoc tests, $p < 0.05$. More details are in the figure legends.

	treatment		Fixed samples				Live samples			
	FHOD3 KD?	FHOD3 AdV?	Avg Sarcomere Number per NRVM	Sarcomere Length (µm)	Z-Line Length (µm)	Thin Filament Length (nm)	Maximal Contraction Velocity (µm/s)	Maximal Relaxation Velocity (µm/s)	Avg % Rhythmic Contractions	Avg % Contracting NRCs in FOV
Mock Knockdown	-	-	12 ± 13	1.71 ± 0.22	1.69 ± 0.43	925 ± 94	7.9 ± 1.6	6.0 ± 1.7	74 ± 9	98.2 ± 3.2
Mock Rescue	+	-	3 ± 7[a]	1.46 ± 0.37[a]	1.38 ± 0.46[a]	n.d.	6.0 ± 1.7[a]	4.4 ± 1.5[a]	14 ± 12	89 ± 11
FHOD3L Rescue	+	+	19 ± 14[a,b]	1.72 ± 0.18[b]	1.70 ± 0.46[b]	739 ± 81[a,b]	7.5 ± 1.5[b]	6.1 ± 1.5[b]	72 ± 20	97.2 ± 4.8
K1193L Rescue	+	+	15 ± 16	1.65 ± 0.22	1.67 ± 0.41	792 ± 79[c]	7.7 ± 1.6	5.9 ± 1.6	88 ± 21	98.2 ± 3.2
GS-FH1 Rescue	+	+	2 ± 4[c]	1.42 ± 0.35[c]	1.23 ± 0.29[c]	n.d.	5.6 ± 1.7[c]	3.6 ± 1.2[c]	3.7 ± 5.2	32 ± 32
FHOD3L Over-expression	-	+	n.d.	n.d.	n.d.	n.d.	6.6 ± 1.6[c]	5.5 ± 1.6[c]	72 ± 21	76 ± 32

Table 2: Summary of FHOD3L and mutant rescue experiments in NRVMs. All data shown are means ± standard deviation each from 3 independent experiments (except for GS-FH1 rescue: maximal contraction and relaxation velocity measurements and average % rhythmic contractions from 2 independent experiments). n.d.= no data. In the lightest columns, "-" indicates treatment with negative control siRNA or empty virus, "+" indicates treatment with FHOD3 siRNA or corresponding FHOD3L adenovirus. Data in the medium-colored columns were acquired from fixed and stained cells. Data in the darkest columns were acquired from live cells. Statistical analyses are described in figure legends.

a- statistically different from mock KD (mock rescue and Fhod3L rescue)
b- statistically different from mock rescue (FHOD3L and GS-FH1)
c- statistically different from FHOD3L rescue (all mutant rescues and overexpression)